R E P O R T

PROBABILISTIC TSUNAMI HAZARD IN CALIFORNIA

Prepared for

Caltrans/PEER

January 5, 2010

566 El Dorado Street, 2nd Floor
Pasadena, California 91101

TABLE OF CONTENTS

SECTION PAGE

1. INTRODUCTION 6
2. TSUNAMI MODELING 7
   - 2.1 Tsunami sources 7
   - 2.2 Tsunami Propagation Model 7
     - 2.2.1 General Linear Gravity Wave 7
     - 2.2.2 Nonlinear Gravity Waves and Shallow Water Waves 9
     - 2.2.3 Numerical Computation 11
     - 2.2.4 Variable grid finite difference 12
3. PROBABILISTIC TSUNAMI HAZARD 12
   - 3.1 Overview 12
   - 3.2 Probabilistic offshore waveheight hazard 13
     - 3.2.1 Overview 13
     - 3.2.2 Green's function summation 13
4. UNCERTAINTIES 14
   - 4.1 Aleatory uncertainties 14
     - 4.1.1 Modeling uncertainty 15
     - 4.1.2 Dip uncertainty 15
     - 4.1.3 Slip variability 15
     - 4.1.4 Total sigma and epsilon truncation 16
   - 4.2 Epistemic uncertainties 16
     - 4.2.1 Sources 16
     - 4.2.2 Logic Trees 17
5. INUNDATION HAZARD 18
6. BATHYMETRY 18
   - 6.1 Bathymetry sources 18
   - 6.2 Global and regional models 19
     - 6.2.1 ETOPO2v2 19
     - 6.2.2 NOAA/NGDC 19
   - 6.3 High resolution local models 19
     - 6.3.1 Crescent City 19
     - 6.3.2 Humboldt Bay 19
     - 6.3.3 San Francisco Bay 19
     - 6.3.4 Monterey Bay 19
     - 6.3.5 Central coast 20
     - 6.3.6 Santa Barbara Channel, Los Angeles and San Diego 20
7. SOURCE MODELS 20

7.1 Overview 20
7.2 Earthquake recurrence rates 21
7.3 Geologic evidence for multi-branch magnitude recurrence 21
7.4 Distant sources 22
7.4.1 Alaska - Aleutian 22
7.4.2 Kamchatka-Kuriles 22
7.4.3 Izu-Bonin-Marianas 23
7.4.4 Ryukyu 23
7.4.5 Philippines 23
7.4.6 Solomon, Vanuatu 23
7.4.7 Chile 23
7.4.8 Peru 24
7.4.9 Central America 24
8. RESULTS 24
8.1 Offshore hazard maps 24
8.2 Inundation hazard 25
8.3 Flow velocity 25
9. DISCUSSION AND CONCLUSIONS 26
10. REFERENCES 27
11. TABLES 31
12. FIGURES 34

TABLES

Table 1 Grids used in the finite difference computations....31
Table 2 Recurrence parameters for major subduction zone earthquakes....32
Table 3 Recurrence model for the Alaska - Aleutian subduction zone....33
Table 4 Recurrence model for the Kamchatka-Kurile subduction zone....33

FIGURES

Figure 1 Finite difference calculation of the tsunami wavefield for the 2004 Sumatra earthquake....34
Figure 2 Example of the rupture parameterization using subfaults....35
Figure 3 Summation of Green's functions. Wavefield for an individual subfault (left). Summation of several subfault Gren's funtions to compute tsunami response (red line) from a compound rupture. 36
Figure 4 Map of the Pacific Ocean showing the source regions used in this study....37
Figure 5 Bathymetric model of California showing the extent of the intermediate (blue boxes) and finest (red boxes) grids....38
Figure 6 Misfit of tsunami simulation with observed data for a coarse grid (top) and a fine grid (bottom). 39
Figure 7 Variability of tsunami amplitudes due to source slip distributions....40
Figure 8 Effect of different sources of uncertainty on the hazard curves at two locations,....41
Figure 9 Effect of epsilon truncation on hazard curves....42
Figure 10 Segmentation model for the Alaska-Aleutian subduction zone....43
Figure 11 Segmentation model for the Kuril-Kamchatka subduction zone....44
Figure 12 Seismic coupling coefficients....45
Figure 13 Offshore exceedance waveheight for a 72 yr return period....46
Figure 14 Offshore exceedance waveheights for a 475 yr return period....47
Figure 15 Offshore exceedance waveheight for a 975 yr return period....48
Figure 16 Ofshore exceedance waveheight for a 2500 yr return period....49
Figure 17 Rupture segment disaggregation for offshore San Diego, 475 yr ARP....50
Figure 18 Rupture segment disaggregation for Santa Monica, 475 yr ARP....51
Figure 19 Rupture segment disaggregation for Port San Luis (Avila Beach), 475 yr ARP....52
Figure 20 Rupture segment disaggregation for the Golden Gate (offshore, Pacific side), 475 yr ARP....53
Figure 21 Probabilistic inundation map for the San Francisco Bay area....54
Figure 22 Probabilistic inundation map of southern Monterey Bay....55
Figure 23 Probabilistic inundation map for Morro Bay....56

Figure 24 Probabilistic inundation map for Pismo Beach. 57
Figure 25 Probabilistic inundation map for the Ventura region. 58
Figure 26 Probabilistic inundation map for Port of Los Angeles to Orange County. 59
Figure 27 Relationship between flow velocity and water column height in inundated areas. 60
Figure 28 Distribution of the ratio between water column height and flow velocity. 61

1. INTRODUCTION

The recent tsunami disaster caused by the 2004 Sumatra-Andaman earthquake (Figure 1) (Ammon et al., 2005) has focused our attention on the hazard posed by large subduction zone earthquakes and the tsunamis that they generate. Even before this destructive event, a significant amount of work was carried out in this field, primarily through deterministic modeling of tsunami scenarios (e.g. Borrero et al., 2005). Such studies often address worst-case scenarios or some type of maximum credible event. In order to put these types of studies on a firm basis, it is necessary to conduct a comprehensive review of tsunamigenic sources that can affect a certain locality, and determine the probabilistic hazard level based on this set of sources. Also, notwithstanding the great usefulness of individual scenario maps, in order to assess the hazard for a certain region, it may be more appropriate to start with a map of the tsunami hazard, analogous to the seismic hazard maps that are published by government agencies such as the United States Geological Survey and statewide agencies in the US, or the Global Seismic Hazard Assessment Program. Even though events like the Sumatra-Andaman earthquake and tsunami are rare, the very large loss of life (> 200,000 dead or missing) and tremendous material destruction over large geographical areas warrant a significant effort towards the mitigation of the tsunami hazard. In recent years, the risk posed by tsunami to United States coastal communities from a variety of sources have also become apparent and the need for a comprehensive and consistent methodology to evaluate this aspect of earthquake risk, which so far has been neglected compared to the attention paid to the hazard from strong ground motion, is obvious. On the other hand, where there is concern about tsunami damage, the lack of a consistent framework to evaluate this hazard has given rise to unnecessarily conservative estimates of the hazard, which can result in an economic barrier to development of coastal communities and facilities.

Given the maturity and widespread acceptance of Probabilistic Seismic Hazard Analysis (PSHA) in seismic hazard mitigation, we believe it would most beneficial to cast our methodology for tsunami hazard mitigation in a similar framework. By exploiting the commonality between tsunami and seismic hazard models, such as the earthquake recurrence models, we assure maximum consistency across the two disciplines, which facilitates the evaluation of the combined hazard posed to coastal communities, facilities and infrastructure.

2. TSUNAMI MODELING

2.1 TSUNAMI SOURCES

In this study we have limited our source model to earthquake sources, which dominate the hazard at shorter return periods. The tsunami excitation by earthquake sources is modeled by translating the vertical deformation field of the earthquake source (surface faulting) into a vertical displacement of the water column. This method is commonly used in tsunami studies (e.g. Titov and Synolakis 1996; Satake 1995). The static displacement fields were computed using a frequency-wave-number integration technique (FK) using a simple layered crustal model (Wang et al., 2003; 2006).

2.2 TSUNAMI PROPAGATION MODEL

We take a Eulerian approach to describe the particle motion of the fluid. Only the velocity changes of the fluid are described at some point and at some instant of time rather than describing its absolute displacement. We consider a wave that is a propagating disturbance from an equilibrium state. Gravity waves occur when the only restoring force is gravity. When the horizontal scale of motion is much larger than the water depth, then the vertical acceleration of water is much smaller than the gravity acceleration and thus negligible. This means that the whole water mass from the bottom to the surface is assumed to move uniformly in a horizontal direction. This kind of gravity wave is also known as a "long-wave." Long wave approximations are appropriate when the water depth of lakes and oceans (< 5 km) is much smaller than the length of the disturbance (fault lengths ~ 10-1000 km). This approximation gives an accurate description of tsunami wave propagation in the open ocean. In order to also model the propagation of tsunami waves in coastal areas, we use an approximation to the wave equation where the low-amplitude linear long-wave requirements are relaxed, as shown in the following sections.

2.2.1 General Linear Gravity Wave

The following is a derivation of the general case of gravity waves for two dimensions where x is the horizontal direction and z is vertical direction. We start from the Euler's equation of motion that considers the conservation of momentum on a volume of water. The Newton equations can be simplified as, (Eq 1.)

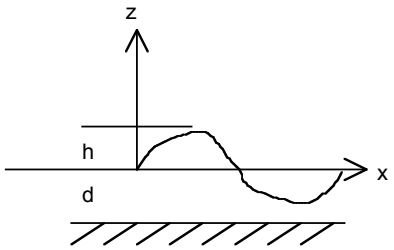

$$\frac{d}{dt}V = g - \frac{1}{\rho}\nabla p$$

where *d/dt* is the total and ∂/∂t is the partial derivative with respect to time, *g* is the gravitational acceleration, V = (*u*,*w*) are the depth averaged velocities in the *x* and *z* directions, ρ is the density, and *p* is the fluid pressure. The figure shows that *h* is the tsunami wave height and *d* is the water depth. We next consider the conservation of mass to derive the equation of continuity,

$$\frac{\partial \rho}{\partial t} + \nabla \cdot (\rho V) = 0$$

and for incompressible fluid becomes,

$$\nabla \cdot V = 0.$$

From the Euler's equation of motion the horizontal and vertical acceleration components are,

$$\frac{du}{dt} = -\frac{1}{\rho}\frac{\partial p}{\partial x}$$

$$\frac{dw}{dt} = -g - \frac{1}{\rho}\frac{\partial p}{\partial z}$$

The relationship between *h* and *p* is related through the hydrostatic pressure equation,

$$p = -\rho g(h - z) + p_0$$

where *h* is the wave height, *z* is the water depth, and p_0 is the pressure of one atmosphere at $z = 0$ and $h = 0$. The horizontal and vertical pressure gradients given from the slope of the water surface,

$$\frac{\partial}{\partial x}p = pg\frac{\partial h}{\partial x}$$

$$\frac{d}{dz}p = -\rho g$$

are combined with the Euler's equation to give the horizontal and vertical components,

$$\frac{du}{dt} = -g\frac{\partial h}{\partial x}$$

$$\frac{dw}{dt} = 0$$

For ocean tsunamis, the non-linear advective term is small and can be ignored, therefore the equation of motion is,

$$\frac{du}{dt} = \frac{\partial u}{\partial t} + u\frac{\partial u}{\partial x} \approx \frac{\partial u}{\partial t}$$
$$\frac{\partial u}{\partial t} = -g\frac{\partial h}{\partial x}$$

We next consider the conservation of mass for a region with a small length *dx*. Since the volume change per unit time must be equal to the flow rate of water going out of this region, we can therefore write

$$\frac{\partial}{\partial t}\{(h+d)dx\} = -\frac{\partial}{\partial x}\{u(h+d)\}dx$$
$$\frac{\partial h}{\partial t} = -\frac{\partial}{\partial x}\{u(h+d)\}$$
$$\frac{\partial h}{\partial t} = -\frac{\partial}{\partial x}(du)$$

which is the simplified equation of continuity when the amplitude of the wave is small compared to the water depth. The so-called small-amplitude, linear, long wave assumption is valid for most of the tsunami propagation paths except near coasts.

2.2.2 Nonlinear Gravity Waves and Shallow Water Waves

Without a viscous force to dissipate wave energy, the water motion will continue forever. In order to include the viscous effect, we can add a term for viscous stress to the equation of motion. We only consider a shear stress at the water bottom and the normal stress is already included and equal to the pressure. The shear stress is experimentally estimated as

$$\tau_x^{\,b} \approx C_f v_x \sqrt{v_x^{\,2} + v_y^{\,2}}$$

and the frictional force is

$$F_x^{\,b} = C_f \frac{v_x \sqrt{v_x^{\,2} + v_y^{\,2}}}{d+h}.$$

Satake [1995] adopted two types of frictional coefficients from engineering hydrodynamics for including bottom friction for tsunamis. These are the De Chezy (C) and Mannings's roughness (n) coefficients. These have different dimensions and therefore a non-dimensional frictional coefficient C_f is related to these two coefficients by

$$C_f^{\,2} = \frac{g}{C_c^{\,2}}$$

and

$$C_f = \frac{gn^2}{(d+h)^{1/3}}.$$

The Manning's roughness coefficient n is used for a uniform turbulent flow on a rough surface. It indicates that the bottom friction varies with water depth. We use an n of 0.03 $m^{-1/3}$ s, typical for coastal waters. If n is translated to C_f, then n becomes 2.3×10^{-3} for a total depth of 50 m and 1×10^{-2} for a total depth of 0.6 m, which agree well with observational values of tidal flow and run-up of solitary waves (see Satake [1995]).

Since the earth is rotating, there is a force apparently acting on a body of water. In an inertial reference frame (fixed on the rotating Earth), this force is called the Coriolis force. The derivation of this term is beyond the scope of this report and we refer the reader to textbooks on analytical mechanics. The vertical component of the Coriolis force is much smaller than gravity (3 cm/s^2 compared to 980 cm/s^2 at 4000 m depth). In a local Cartesian coordinate system, the horizontal components are given by

$$F_x^{cor} = -fv_y$$
$$F_y^{cor} = fv_x$$

where f is the Coriolis parameter, and this force always acts to the right hand side of the motion in the northern hemisphere. The Coriolis force is only significant for long propagation times and distances along lines of latitude near the equator.

We derive the equations for general gravity waves without making the small amplitude, linear long-wave approximation appropriate when the wave height is much smaller than the water depth (h<<d). If we expand the hyperbolic tangent function using the Taylor series expansion and include the first and second order terms then the corresponding equation of motion becomes

$$\frac{\partial u}{\partial t} = -g\frac{\partial h}{\partial x} + \frac{1}{3}d^2\frac{\partial^3 u}{\partial x^2 \partial t}$$

which is also known as the Boussinesq equation. After relaxing the small amplitude assumption, the equation of motion and continuity are given as

$$\frac{du}{dt} + u\frac{\partial u}{\partial x} = -g\frac{\partial h}{\partial x}$$
$$\frac{\partial h}{\partial t} = -\frac{\partial}{\partial x}\{u(h+d)\}$$

These equations are for the finite-amplitude shallow water waves. For the linear case, the phase velocity is given by the following Taylor series expansion of the hyperbolic tangent function,

$$c = \sqrt{gd}\left\{1 - \frac{2\pi^2}{3}\left(\frac{d}{\lambda}\right)^2\right\},$$

where λ is the wavelength. In the nonlinear case the d-term in the phase velocity is replaced by the total height of the water column (d+h) which gives us a phase velocity of the form

$$c \sim \sqrt{g(d+h)}$$

Note that in the nonlinear case a phenomenon of amplitude dispersion occurs, the larger the amplitude, the faster the wave speed. As a consequence, peaks of a wave catch up with troughs in front of them, and the forward facing portion of the wave continues to get steeper. This wave will eventually break.

Including the bottom friction and Coriolis force, the equation of motion for shallow water waves can be written for a two-dimensional case as follows:

$$\frac{\partial U}{\partial t} + U\frac{\partial U}{\partial x} + V\frac{\partial U}{\partial y} = -fV - g\frac{\partial h}{\partial x} - C_f \frac{U\sqrt{U^2+V^2}}{d+h}$$

$$\frac{\partial V}{\partial t} + U\frac{\partial V}{\partial x} + V\frac{\partial V}{\partial y} = -fU - g\frac{\partial h}{\partial y} - C_f \frac{V\sqrt{U^2+V^2}}{d+h}$$

and the equation of continuity is

$$\frac{\partial h}{\partial t} + \frac{\partial}{\partial x}\{U(h+d)\} + \frac{\partial}{\partial y}\{V(h+d)\} = 0$$

where the coordinate system is x=East y=South, f is the Coriolis parameter, C_f is a non-dimensional frictional coefficient, and U and V are the average velocities in the x and y directions, respectively. The first term on the left hand side (lhs) is the local acceleration term, the second and third terms on the lhs are the advection terms, the first term on the right hand side (rhs) is the Coriolis force, the second term on the rhs is the restoring force from gravitation acceleration, and the third term on the rhs is the bottom friction force.

2.2.3 Numerical Computation

The equations of motion and equation of continuity are converted from Cartesian to a spherical coordinate system $(x,y,z)\rightarrow(r,\theta,\varphi)$ with the origin at the Earth's center, but r is constant and equal to the Earth's radius R. Note that θ is the co-latitude and measured southward from the North Pole and φ corresponds to longitude measured eastward from the Greenwich meridian. These equations are solved by finite-difference method using the staggered leapfrog method (e.g., Satake, 1995). For the advection terms, upwind difference scheme is used (e.g., Press et al., 1992). The land-sea boundary condition in the linear computation is total reflection and in the nonlinear case there is a moving boundary condition and run-up is considered. The time step of computation is determined to satisfy the stability condition (Courant condition) of the linear, and by trial and error for the nonlinear, finite-difference computations.

2.2.4 Variable grid finite difference

The variable grid setup consists of a master grid with a coarse grid spacing and a number of nested finer grids with decreasing grid sizes around areas of interest. Our code allows for more than one area with decreased grid size, which we used for our smallest grids, as shown in Figure 5. In this model, the deep ocean part is sampled at 120 arc seconds. Because of the very long wavelength of the tsunami waves in the deep ocean, such a sampling is sufficient for accurate results and reduces the computation time and memory requirements considerably. Closer to shore, we used several nested grids stepping down to 4.8 arc sec (approx 150 m). The timestep for these runs is 0.2 sec. Currently, our code uses a fixed timestep, which generally is controlled by the finest gridsize.

3. PROBABILISTIC TSUNAMI HAZARD

3.1 OVERVIEW

Probabilistic Seismic Hazard Analysis (PSHA) has become standard practice in the evaluation and mitigation of seismic hazard to populations in particular with respect to structures, infrastructure and lifelines. Its ability to condense the complexities and variability of seismic activity into a manageable set of parameters greatly facilitates the design of effective seismic resistant buildings but also the planning of infrastructure projects. Probabilistic Tsunami Hazard Analysis (PTHA) achieves the same goal for hazards posed by tsunami. Although this field is not very developed yet, we believe there are great advantages of implementing such a method to evaluate the total risk (seismic and tsunami) to coastal communities, facilities and infrastructure.

Previous work on PTHA includes Downes and Stirling (2001) who proposed to use an empirical attenuation relation similar to ground motion attenuation relations. They recognize that such attenuation relations would have to be source and site specific, and we believe it doubtful whether there would ever be enough data available for such attenuations relations to be derived consistently. On the other hand, Geist and Parsons (2005) developed a method that uses the full linear calculations for a limited number of scenarios for earthquakes near the site. The main difference with their work is that through the Green's function summation, we can generate many more fault scenarios and at arbitrary distances including teleseismic, which allows us to run full probabilistic analyses over a much wider area (Burbidge et al., 2008). Also, our method is very efficient for the analysis of many sites simultaneously, which allows us to quickly identify areas at elevated risk. Such information is indispensable for the effective allocation of funds for tsunami hazard mitigation work.

The method that we have developed is based on the traditional PSHA and therefore completely consistent with standard seismic hazard practice. It provides an overview of the tsunami hazard along entire coastlines, and helps identify the specific tsunami source regions for which a particular site on the coastline is sensitive to.

3.2 PROBABILISTIC OFFSHORE WAVEHEIGHT HAZARD

3.2.1 Overview

The methodology behind PSHA is well known (e.g. McGuire, 2004) and here we will only briefly describe the adaptations that are made for PTHA. Whereas in PSHA we are usually interested in the exceedance of some ground motion measure such as Peak Ground Acceleration (PGA) or Spectral Acceleration (SA), in PTHA a parameter of interest (not necessarily the only one) is the maximum tsunami height that is expected to be exceeded at sites along the coast. The statistical earthquake model behind the two methods is the same, the only difference being that in PTHA we are not concerned with earthquakes that are completely inland. The difference between the two methods lies in the part that in PSHA is referred to as attenuation relations. These relate a certain moment release on a fault (or an area) to the ground motion parameters as a function of distance. Because of the strong laterally varying nature of tsunami propagation, we have adopted a waveform excitation and propagation approach instead of trying to develop analogous tsunami attenuation relations. In fact, current developments in traditional PSHA include the replacement of the attenuation relations with ensembles of numerically generated ground motions, which is entirely analogous to the approach that we propose here.

The excitation and propagation of tsunamis in deeper water can be modeled using the shallow water wave approximation, which, for amplitudes that are significantly smaller than the water depth, are linear (Satake, 1995). We can solve the equation of motion numerically using a finite-difference method (Figure 1), which has been validated to produce accurate tsunami heights for propagation through the oceans, although for very shallow water the amplitudes may become too large and more sophisticated non-linear methods are required to model the details of the run-up accurately. Nevertheless, the linear approach provides a very good first approximation of tsunami propagation, taking into account the effects of lateral variations in seafloor depth.

3.2.2 Green's function summation

The underlying principle for this approach is the validity of the linear behavior of tsunami waves. This enables us to deconstruct a tsunami that is generated by an earthquake into a sum of individual tsunami waveforms (Green's functions) from a set of subfaults that adequately describe the earthquake rupture (Figure 2). By pre-computing and storing the tsunami waveforms at points along the coast generated by each subfault for a unit slip, we can efficiently synthesize tsunami waveforms for any slip distribution by

summing the individual subfault tsunami waveforms (weighted by their slip) (Figure 3). The same principle is used in the inversion of tsunami waves for earthquake rupture (e.g. Satake, 1995). This efficiency makes it feasible to use Green's function summation in lieu of attenuation relations to provide very accurate estimates of tsunami height for probabilistic calculations, where one typically needs to compute thousands of earthquake scenarios. For instance, in the example below the probabilistic tsunami heights results are based on more than ten thousand scenarios, which were computed (using the Green's functions summation) on a 30-node cluster computer.

The assumption of linearity is not valid for tsunamis where the amplitudes are comparable to the water depth. Also, the detailed bathymetry near the shoreline is important to estimate the final run-up heights. For these cases, a non-linear method is necessary to compute the run-up heights correctly. However, several authors have proposed simple corrections that can be applied to the tsunami heights that are calculated with a linear code. Our first concern will be in computing the tsunami response from a number of sources (Figure 4) to a particular depth contour (e.g. 15 m) off the California coastline (Figure 5).

4. UNCERTAINTIES

An inherent part of a probabilistic hazard analysis is the inclusion of uncertainties in the underlying models (both source and propagation) into the final result itself. Based on the character of an uncertainty, we distinguish between two types: aleatory and epistemic uncertainty.

4.1 ALEATORY UNCERTAINTIES

Aleatory uncertainties, in a strict sense, reflect our inability to predict the outcome of a process due to its random nature. Whether or not an uncertainty in the outcome of a process is a true aleatory uncertainty, i.e. caused by the random behavior of nature rather than our limited understanding of the process itself, is not always clear. In practice, this distinction is not important. Aleatory uncertainties are typically accounted for by the use of distribution functions rather than a single mean or median values to express the outcome of a process. The probability of an outcome being in a certain range is then given by the area under the probability density (or distribution) function. In our analysis we have identified three main contributions to the aleatory uncertainty: modeling uncertainty (σ_A), uncertainty in dip (σ_D) and uncertainty to random slip distribution (σ_S).

4.1.1 Modeling uncertainty

Under modeling uncertainty, we include the mismatch, given known source parameters, between observed and computed tsunami waveforms. Several different sources contribute to this modeling uncertainty, the two most important being errors from the numerical implementation (i.e. our finite difference scheme) and errors from shortcomings in the bathymetric model (either errors in the model, or insufficient resolution). We have estimated this uncertainty by modeling several large and well-constrained tsunamis along the California coast, including 1960 Chile, 1964 Alaska and the 2006 Kurile event and comparing the observed and computed maximum waveheights or runups. The results are summarized in Figure 6, where we show the combined misfit data (after removal of bias) for simulations using a coarse grid (2 km) and a fine grid (90 m). Since the fine grid computations were confined to smaller areas, the dataset is much smaller, but it is nevertheless clear that the fine grid computations show a significantly smaller standard deviation than the coarse grid computations. The standard deviations (σ_A) for the coarse and fine grids are 0.595 and 0.345 (natural log) respectively. The bias in the fine grid computations is negligible, and for the individual events are distributed around zero. For the coarse grid, there is a positive bias in all simulations, but this will be eliminated once we compute the inundation hazard using the fine grids.

4.1.2 Dip uncertainty

Since the variations in dip have a direct impact on the vertical deformation of the seafloor and thus the height of the resulting tsunami we have included this as a separate term in our analysis. Also, since our offshore waveheight hazard is based on pre-computed Green's functions, which have a fixed dip at the source, we include here uncertainties in the overall dip of the source, which would normally be included as an epistemic uncertainty. That approach would necessitate the computation of a multitude of Green's functions over the current set, which would make this analysis too expensive in terms of computation time and storage. Rather, we have chosen to determine a single distribution function that represents the effects of dip variation by modeling scenario waveforms for a distribution of the dip angles around a mean (10 degree dip, with a standard deviation of 5 degrees). This results in a standard deviation (σ_D) of 0.292.

4.1.3 Slip variability

We computed σ_S in the same way as the contribution from the dip variations, by iterating over a large number of different slip distributions with equal magnitude. Although our Green's function approach allows us to include slip variability directly into the hazard computations, we have chosen to include this effect as a sigma term since a) the slip variability is really an aleatory uncertainty and, b) in order to

sample the distribution sufficiently, we would probably have to iterate over a large number of slip distributions for every singe source in our event set. The results are shown in Figure 7, with a σ_S of 0.256

4.1.4 Total sigma and epsilon truncation

Based on the aforementioned sigma terms we compute a total sigma using:

$$\sigma_{total} = \sqrt{\sigma_A^2 + \sigma_D^2 + \sigma_S^2}\,.$$

The offshore waveheight is computed using a coarse grid and it would therefore follow that we should be using the coarse grid version of σ_A to compute the total standard deviation. However, as we will be using the offshore waveheights only with the purpose of using it as an intermediate step to compute the final waveheight and inundation using the fine grids, we feel it is more appropriate to use the fine-grid sigma instead. The total sigma is therefore 0.519.

Because of the unbounded nature of the normal distribution it is common in seismic hazard analysis to truncate the distribution at a certain number of standard deviations (epsilon). A typical value for epsilon truncation is 3, i.e. we don't allow for ground motions (or in our case waveheights) that are more than three times the standard deviation away from the mean. In Figure 9 we present a comparison between hazard curves for different truncation levels (2, 3 and 4). It is clear that in this range of probabilities the difference between epsilon 3 and 4 are very small, whereas there are some differences between 2 and 3. We therefore decided to use an epsilon of 3 for truncation of the maximum waveheights in the probabilistic analysis.

4.2 EPISTEMIC UNCERTAINTIES

As already mentioned, uncertainties due to an incomplete understanding of natural processes are called epistemic uncertainties, and the way these uncertainties are incorporated is fundamentally different than the way aleatory uncertainties are included. In our analysis, the following uncertainties are deemed epistemic:

- Fault segmentation (single or multi-segment ruptures)
- Slip rate (actual slip rate or fraction of slip seismogenic slip rate)
- Recurrence model (use maximum magnitude or Gutenberg-Richter model, slip rate based versus direct earthquake recurrence rate)

A comprehensive account of the different elements will be given in the next section.

4.2.1 Sources

A crucial element in PTHA is the estimation of the maximum magnitude, and its probability, for any source region. Due to the very short historic record for mega-thrusts and other large earthquakes in

relation to their recurrence times, it is not possible to base any such constraint on the directly observed seismicity. We therefore need to resort to models that are at least partly based on earthquake mechanics, which can be as simple as magnitude/area relations but can also include physics-based constraints in addition to empirical data such as earthquake locations. Uncertainties in source parameters, such as maximum earthquake and slip rate, are included using logic tree analysis. Other approaches toward PTHA often use a limited range of deterministic scenarios with associated probabilities or return periods, sometimes in combination with historical tsunami records (Berryman, 2006; Imamura et al., 2006; Geist and Parsons, 2006).

4.2.2 Logic Trees

The discrete nature of the epistemic uncertainties is expressed through the use of logic trees, where all the different manifestations of a process are represented as a branch of a logic tree.

Uncertainties in the model parameters are generally incorporated using a logic-tree approach, where different alternatives are represented as weighted branches. These include variations in slip-rate, magnitude range and distribution, fault geometry as well as rake. As already mentioned, dip variations would normally also be considered under the epistemic uncertainties, but due to the fact that these would require a new set of Green's functions, we have added these as an aleatory uncertainty.

In the Green's function approach, it is convenient to divide these uncertainties into two groups, viz. parameter variations that act on the Green's function level (e.g. fault geometry) and parameters that do not influence the Green's functions, such as the recurrence parameters and magnitude scaling relations. In the latter case, the logic tree branches are easily added without major computational requirements but for the former, the question is whether any extra branch in the logic tree, such as a variation in slip, would require an entire set of Green's functions. From some simple numerical experiments, we conclude that in many cases, especially at large distances, these variations can accurately be taken into account by perturbing the Green's functions using a constant scaling factor rather than re-computing them. For example, a change in rake, readily translates into a change of the vertical seafloor displacement, which in turn directly translate in differences in waveheight.

At shorter distances, i.e. local faults, this approach is less accurate, and in these situations (particularly for dip-slip events) we will have to resort to complete re-computation of the Green's functions. However, since these sources are relatively scarce, and require less computing time due to the short distances, this is far less of a burden than having to re-compute tele-tsunami Green's functions.

5. INUNDATION HAZARD

In order to extend the offshore waveheight hazard to inundation hazard, we chose to use a numerical approach rather than existing empirical approaches because of the limitation in accuracy of the latter. We used the source disaggregation for several regions along the California coast to select the source regions, and magnitudes that contribute the most to the hazard. Invariably, apart from the contribution of the Cascadia subduction zone on the Cascadia hazard, only three other regions are very significant: Alaska, Kamchatka-Kurile and Chile. All subsequent scenarios were therefore done for these regions. Just using the disaggregation to select the scenarios is not sufficient since this would not include the aleatory uncertainties in the offshore waveheight. We therefore computed a suite of scenarios with increasing amplification factors (i.e. we multiplied the slip by increasing factors) and for every region and return period chose the scenarios that yielded waveheights that bracket the probabilistic offshore waveheights. This matching is carried out using the coarse grid from the non-linear runs (which is similar to the coarse grid from the probabilistic offshore hazard calculations) so that differences in bias between the fine grids and coarse grids are taken into account.

The inundation from that particular source region can then be determined by taking the weighted average of the two scenario runs that bracket the offshore waveheight. This way, we only need to compute a limited number of fully non-linear scenarios but still retain the directional (i.e. source region specific) character and probabilistic nature of the hazard. The line of inundation can then be determined by specifying that it borders an area that is inundated by tsunami waves from all the different major source zones for that particular return period. In addition, we can also compute the local inundation level (height of the water column) exceedance for different return periods.

6. BATHYMETRY

6.1 BATHYMETRY SOURCES

Because of the large range of grid resolutions and large geographic areas involved, we have used a varied set of data sources for modeling the tsunami waveforms. This potentially poses a problem of continuity, but in the case of North America this is not as severe as most bathymetry models, including the global models, are based on NOAA's 90m nearshore bathymetry. The grid setup used in the inundation hazard analysis is shown in Figure 5.

Current high-resolution mapping efforts are underway by NOAA of several areas along the west coast for tsunami inundation purposes. The resolution is 1/3 arc seconds, or about 30 m, and we have used these models as far as they were available at the time of our modeling (Monterey Bay, Port San Luis).

6.2 GLOBAL AND REGIONAL MODELS

6.2.1 ETOPO2v2

A global model published by the National Oceanographic and Atmospheric Agency (NOAA) is based on a combination of gravity-derived bathymetry, bathymetric surveys (including GEBCO) and the NOAA nearshore model. At a resolution of 2 arcsec (approx. 4 km), this model is suitable for deep ocean propagation. In general, its accuracy in nearshore areas is rather poor but for the United States, since it used the NOAA nearshore database, the model is adequate at the resolution used.

6.2.2 NOAA/NGDC

NOAA has released a 9 arcsec grid of all the nearshore areas of the United States (Divins and Metzger, 2007). These grids are regularly updated, and the version used in this analysis was released in 2007. The model is based on shiptrack data and soundings and is generally quite accurate for nearshore areas. However, at the shoreline, the accuracy is not as high, which requires us to use local elevation models for the actual inundation modeling.

6.3 HIGH RESOLUTION LOCAL MODELS

These grids are shown as subgrids in Figure 5. They were derived from a variety of sources which are described below.

6.3.1 Crescent City

30 meter bathymetry from NOAA was made available to us courtesy of Dr. B. Uslu (University of Southern California, now at NOAA).

6.3.2 Humboldt Bay

Detailed bathymetry of Humboldt Bay has been made available by the CICORE project (5 m resolution) based on LIDAR and other methods.

6.3.3 San Francisco Bay

The USGS http://sfbay.wr.usgs.gov/sediment/sfbay/index.html provides this high-resolution data, used for marine studies of the San Francisco Bay at a resolution of 100 m for the entire Bay, and 50 m for several areas inside the Bay.

6.3.4 Monterey Bay

This area has been mapped extensively by the Monterey Bay Aquarium Research Institute (MBARI), whose model is included in the Monterey Bay grid (1/3 arcsec) of the NOAA Tsunami Gridding Project.

6.3.5 Central coast

This area is covered by the NOAA Tsunami Gridding Project (Port San Luis grid) with some additional outlying parts derived directly from the NOAA nearshore grid.

6.3.6 Santa Barbara Channel, Los Angeles and San Diego

For these areas the best models available are the NOAA nearshore grid.

7. SOURCE MODELS

7.1 OVERVIEW

In probabilistic analyses, the rate of occurrence of earthquakes is of prime importance for the computation of the hazard. Constraints for these occurrence rates typically come from the observed seismicity record, and from tectonic considerations such as average deformation rates along plate boundaries.

The recurrence models used for the seismic hazard maps tend to favor the recurrence of earthquakes in individual fault segments, which limits the maximum magnitude to that allowable by the dimensions of the segments. The segmentation models are based on the slip distribution of historical earthquakes and a drawback of this approach is that our historical record may be too short to sample very large earthquakes that rupture entire subduction zones, or at least multiple segments, since they occur rarely. This may not be a very significant problem in shaking hazard, since the high frequency ground motions tend to saturate for larger magnitudes. For tsunamis however, amplitudes continue to grow with magnitude even for giant earthquakes, and we therefore need to address the possibility of giant earthquakes. Until the occurrence of the 2004 Sumatra earthquake, the prevailing scientific opinion regarding giant subduction zone earthquakes was that they only occur where young oceanic crust is being subducted at high rates. The Sumatra-Andaman subduction zone did not fall into that category, and the devastating 2004 event upended this common wisdom. Since then, geologic evidence from several parts of the world have shown that in some subduction zones, the major stress release takes place both through M=8 events on individual segments, at relatively short intervals (~100 yrs), as well as giant multi-segment events with much longer recurrence times (~500 - 1000 yr) that have not been observed historically.

Statistical considerations also indicate that our current view is biased toward these M=8 events since they occur more frequently and that we currently cannot rule out giant events that break entire subduction interfaces.

Our logic trees usually consist of two main branches, one where the plate boundary breaks in smaller, single-segment events as often has been observed in the historical record, and a branch where the

maximum sized earthquake (based on fault dimensions) is considered. In Table 2 we present the predicted maximum magnitudes and the historically observed largest magnitudes for all large subduction zones.

7.2 EARTHQUAKE RECURRENCE RATES

To estimate the recurrence rates of subduction zone earthquakes, we typically rely on two lines of evidence, which are both in their own way quite imperfect. The most direct evidence would be the actual historical record of tsunamis, or at least subduction zone earthquakes. The problem here, as in seismic hazard, is that the historical record is very short compared to the recurrence time of large earthquakes, especially the giant subduction zone events. Geological studies of tsunami deposits can extend this record extensively (e.g. Atwater and Moore 1992; Satake et al., 1996; Sieh, et al., 2003; Nanayama et al., 2003; Pinegina,et al., 2003; Cisternas et al., 2005) but currently the geographical extent of these studies is rather limited. The 2004 Sumatra earthquake and tsunami has given a fresh impetus to studies of the geological record of tsunamis and some interesting results have already been found regarding previous events along the same structure (Jankaew et al., 2008).

Alternatively, we can estimate recurrence rates by using convergence rates from plate models and assuming that convergence is primarily accommodated by seismic release. This is regular practice for crustal faults in seismic hazard analysis but it appears that in subduction zones only a fraction of the total convergence rate is released in earthquakes. The seismic coupling coefficient, which is the ratio between the seismic slip rate and the total slip rate, has been the subject of several studies. Pacheco et al. (1993) computed coupling coefficients for all subduction zones and found that the coupling coefficient, based on 90 years of observations, is very low for most subduction zones (Figure 12). A low coupling coefficient could simply be the result of the return time being much longer than 90 years, but McCaffrey (1997) concluded, on the basis of a statistical analysis that the observed earthquake recurrences can be explained, on a worldwide basis, with a single coupling coefficient of 0.3. In our models, we have used larger coupling coefficient in some cases where we believe the historical record warrants it. However, this area of the analysis remains poorly constrained.

7.3 GEOLOGIC EVIDENCE FOR MULTI-BRANCH MAGNITUDE RECURRENCE

One of the most vexing problems in probabilistic hazard analysis is the correct identification of the event recurrence. In this report we used two main types of recurrence relations, truncated Gutenberg-Richter (G-R) and Maximum Magnitude. The distribution function for the Gutenberg-Richter relations shows an exponential decay of number of events with magnitude, whereas the Maximum Magnitude model is represented by a normal distribution around the Maximum Magnitude. For large fault systems, especially at subduction zone interfaces, the Maximum Magnitude is often used, e.g., Annaka et al., 2007; Geist

2008. Even if globally the distribution of earthquakes for very large magnitudes follows a G-R relation, this does not imply that a GR relation would be appropriate for recurrence relations on a single interface. The global GR relation could be a manifestation of a size distribution of subduction zone interfaces, which at a local level would be consistent with a Maximum Magnitude distribution.

M_{Max}, and thus the maximum slip that can occur, affects the probabilistic tsunami hazard in two opposite ways; larger slip will result in longer recurrence since it will take more time to accumulate the amount of slip, and tsunami waveheight is proportional to the vertical deformation and thus the slip of an event. The latter is not true in seismic hazard where the ground motions tend to saturate with large magnitudes, so that the probabilistic shaking hazard actually declines with increasing M_{Max}.

Geologic evidence points to subduction zone earthquakes occurring on quite different scales, sometimes rupturing single segments, sometimes multiple segments. Along the Kuriles, Nanayama et al. (2003) inferred historic ruptures along the Kurile subduction zone that spanned multiple segments (in this case, at least the Tokachi-Oki and Nemuro-Oki segments). Similarly, along the Alaska subduction zone Shannen et al. (2009) found that the previous ruptures along the 1964 segment also included rupture of the neighboring Yakutat segment. Schwarz (1999) argued on the basis of seismological analysis of several large subduction zone earthquakes that their repeated ruptures are complex and not characteristic, with subsequent earthquakes re-rupturing sections of previous large events. Other observations of multiple segment ruptures are presented below with the individual source descriptions.

7.4 DISTANT SOURCES

7.4.1 Alaska - Aleutian

The Alaska-Aleutian subduction zone marks the boundary between the Pacific and North American plates, and has a strong curvature resulting in very different convergence rates between the eastern and central segments with convergence rates on the order of 60-70 mm/yr and the western segment, where the movement becomes predominantly strike-slip. The historical record of events yields a seismic slip rate that is significantly smaller than that, and the recurrence times in the USGS hazard map for Alaska reflect this fact. The USGS model is strongly segmented based on historical evidence (Figure 10, Table 3). This limits the maximum magnitude, which we feel is not warranted based on the short history (in comparison to return periods of giant earthquakes) and recent studies (Shannen et al., 2009). We therefore decided to introduce several logic-tree branches for the fault segmentation and this maximum magnitude.

7.4.2 Kamchatka-Kuriles

The Kamchatka-Kuriles system stretches from the Aleutian trench to the north end of Honshu, and has experienced some of the largest earthquakes observed worldwide. The historical and geological tsunami record for Hokkaido is quite extensive, and contains evidence for single segment as well as multi-segment

ruptures. As in Alaska, we used the existing recurrence models but added a second logic tree branch that incorporates multi-segment ruptures (Figure 11, Table 4).

7.4.3 Izu-Bonin-Marianas

The boundary between the Pacific Plate and the Philippines Sea Plate shows a large variation in convergence rate, from 50 mm/yr in the north to 0 to the south due to the fact that the PA-PS rotation pole is located almost on the plate boundary. Very few large earthquakes have occurred along this plate boundary, which has been interpreted as being due to very weak coupling between the plates (Kanamori, 1977). We have chosen a coupling coefficient of .25 for this boundary with a maximum magnitude of 8.6 for the dominant branch (85%) and 9.2 for the second branch.

7.4.4 Ryukyu

The northern end of the Ryukyu system is included in the Japanese National maps and consists of the Tonankai, Nankaido and Tokai earthquake zones which have a relatively well-documented history of rupturing, both in single segments as well as multiple segments. We followed the Japanese National Map for the recurrence model, which has maximum magnitudes ranging from 8.1 for the single Tonankai segment to 8.5 for the joint segments.

7.4.5 Philippines

The Philippines trench has a history of large earthquakes with recurrence times of less than a century, but no very large interface events that have generated significant tsunamis at teleseismic distances. Our model uses a convergence rate of 60 mm/yr and a coupling coefficient of .5. For the maximum magnitudes we used two equally weighted branches, with 8.0 based on historical seismicity and 9.4 based on the total extent of the subduction zone (McCaffrey, 2009).

7.4.6 Solomon, Vanuatu

These subduction zones are not thought to have a significant impact on the west coast of North America. We modeled them using convergence rates of 80-100 mm/yr, and coupling coefficients of .5. Maximum magnitudes are 8.2 and 9.1 for the Solomon Islands and 8.5 and 9.4 for the Tonga-Kermadec trench.

7.4.7 Chile

The 1960 Chile earthquake (M_W=9.5) still ranks as the largest recorded earthquake and caused significant tsunamis along the California coast, in particular at Crescent City. Geologic evidence suggests that this interface does not always break in the giant events, but also in smaller events (Cisternas et al., 2005). We therefore chose equal weighted branches with magnitudes of 8.9 and 9.5. The convergence rate is 80 mm/yr, and in this case we have chosen a large coupling coefficient of .8 since this plate interface has shown extensive activity over the last few centuries (Cisternas et al., 2005).

7.4.8 Peru

Along the Peru trench, Okal et al. (2006) found recurrence rates of large earthquakes around Pisco in the 50 – 100 year range, with the subduction of the Nazca ridge seemingly limiting the extent of the earthquake ruptures by acting as a barrier. However, they also concluded that a very large earthquake that occurred in 1868 probably broke through the barrier. They estimate a recurrence time for such a large event (M=9.4) to be on the order of 500 years, with a recurrence on the order of 100 - 250 years for smaller events (M=8.5) that do not break through the barrier.

7.4.9 Central America

The contribution from the Middle America Trench zone to the observed tsunami record in California is low due to the geometry of the subduction zone relative to California as well as the lack of very large earthquakes along this boundary. The largest recorded events are the 1932 and 1995 Jalisco earthquakes (M_S=8.1 and M_W=8.0 respectively) and the 1985 Michoacan earthquake (M_W=8.1) and in general the interface tends to break in smaller earthquakes (7 < M < 8). Recently however, Suárez and Albini (2009) presented evidence for a very large (M=8.6) earthquake that occurred in 1787 in southern Mexico and ruptured at least 4 previously identified asperities. Whereas the single asperity event have return times on the order of a century or less, it appears that the timescale of the very large earthquakes, given the fact that only one has been observed along the entire trench over the last 3 centuries, is probably more on the order of 500 to 1000 years.

8. RESULTS

8.1 OFFSHORE HAZARD MAPS

We have computed probabilistic tsunami wave heights (offshore) for the coast of California based on subduction zone sources around the Pacific Ocean. These results are shown in Figures 13-16, for typical return periods used in engineering. It should be noted that the hazard off the Cascadia subduction zone is not accurate due to the simplifications used for the Cascadia subduction zone, although the contribution of the Cascadia subduction zone to the rest of the state is consistent with the other tsunami sources. Since these are offshore waveheights, it is difficult to interpret their impact directly, since it strongly depends on the run-up properties from the offshore location (around the 15 m bathymetry contour) to the shoreline and beyond, which are heavily dependent on the local bathymetry/topography. However, we can identify some systematic changes of the tsunami hazard along the coast. The wave height patterns show relatively high hazard levels along the north and central coast, which are directly exposed to the Pacific Ocean and

lower levels elsewhere along the coast of Southern California, which is due to blockage by the Continental Borderland. This pattern is particularly clear at the longer return periods.

The value of these maps is that they serve as input to the next stage of our analysis, the inundation mapping. They serve both as a reference waveheight level, which the inundation mapping has to match, as well as a screening tool, by showing us the significant source contributions to the hazard along the coast. For this end, we are showing disaggregation maps in Figure 17-20, for selected locations and return periods. From these maps, it is clear that the Alaska subduction zone dominates the hazard along the California coast south of Cape Mendocino. Other significant sources are the Kurile-Kamchatka subduction zone and the Chilean subduction zone.

8.2 INUNDATION HAZARD

The probabilistic wave heights are very useful tools in assessing the hazard posed by tsunamis. However, as mentioned before, the current approach that allows computation of thousands of scenario tsunamis efficiently is not suited for detailed (non-linear) inundation studies. In contrast to earlier modeling efforts, in which scenarios represented some loosely defined maximum credible event, these scenarios are firmly based on a probabilistic analysis, and represent an event with a specific hazard level.

Using the aforementioned source disaggregation and offshore waveheight matching, we have been able to compute probabilistic inundation maps (Figure 21-26). These maps show for different return periods the extent of flooding due to tsunamis. The maps show inundation for very long return periods, but we consider that these results are valid for return periods of up to 2500 years with the current set of sources. At the resolution of these maps (approximately 150 m) the inundation does not appear very significant in these maps for the shorter return periods, with the exception of the some low-lying coastal areas in and wetlands. At 2500 year ARP however, we find more significant inundation along the coast in Central California (Figure 24), Ventura County (Figure 25) and Orange County (Figure 26) with inundation distances of several hundred meters to several kilometers.

8.3 FLOW VELOCITY

Our main concern in this study has been the determination of waveheight hazard, and in particular inundation hazard. This may be the most important parameter in terms of life safety, but for engineering purposes the effects on structures and foundations are strongly dependent on flow velocity as well. How the two parameters combine to impact a structure probably depends on the type of damage that occurs. One can imagine that the impact on an exposed structure such as a wall or column depends on the total local momentum of the tsunami, which is a combination of water column height and flow velocity, is

important, whereas in other cases, such as scouring around foundations, just the flow velocity is probably most important. The relationship between flow velocity and waveheight is not straightforward, but generally speaking at any point in the model the maxima in waveheight and flow velocity do not occur at the same time. In order to evaluate the interplay of flow velocity and water height we have plotted these two parameters for a large number of grid points and times against each other (Figure 27). Here, we see that the numerical values of water height (in meters) and flow velocity (in meters per second) are of the same magnitude. There is a large spread between the ratios (also seen in Figure 28) but the values are confined in a limited area. Note that these results are strictly for inundation areas, not for general tsunami waves in the open ocean. The average ratio between water column height and flow velocity is 4.82 (Figure 28), which means that the numerical value of velocity is roughly 20% of the water height. The velocity seldom exceeds the water height and the ratio is clearly truncated at high velocities (10 times the water height) and less so at the low velocities, which is as expected.

9. DISCUSSION AND CONCLUSIONS

We have developed probabilistic tsunami inundation maps for California based on tele-tsunami sources. These maps, to our knowledge, represent the first probabilistic analysis of the tsunami hazard in the State, and show localized significant inundation hazard for return periods of up to 2500 years. These maps are based on a hybrid method that matches results from a fully probabilistic offshore waveheight analysis with deterministic inundation modeling. Both aleatory as well as epistemic uncertainties are included in the analysis, and are carried over into the inundation maps.

Although we present inundation maps up to 5000 years ARP, we believe that these results are complete up to 2500 years. Also, along the northern coast of California, north of Cape Mendocino, the results are not accurate since the proximity of the Cascadia subduction zone requires a more comprehensive integration over source variability, rather than including it in an aleatory component, as well as a consideration of vertical movements of the coastline. At return periods longer than 2500 years, we believe that in the rest of the state local offshore faults may also contribute (e.g. Borrero et al., 2004), even if most of them are of a strike-slip nature. Therefore, we have decided that the local sources such as the Cascadia subduction zone will be analyzed in a follow-up study. Beyond the current return periods, it is likely that submarine landslides need to be addressed as well (e.g. Watts, 2004; Locat et al., 2004), which is outside the scope of the present study.

10. REFERENCES

Annaka, T, K Satake, N Shuto, T Sakakiyama, K Yanagisawa, 2004. Logic-tree Approach for Probabilistic Tsunami Hazard Analysis and its Applications to the Japanese Coasts, Abstract: 2004 Fall AGU meeting.

Atwater, B.F., and Moore, A.L., 1992, A tsunami about 1000 years ago in Puget Sound, Washington: Science, v. 258, p. 1614-1617.

Bird, P., 2003. An updated digital model of plate boundaries, Geochemistry Geophysics Geosystems, 4(3), 1027, doi:10.1029/2001GC000252

Borrero J. C., M. R. Legg, C. E. Synolakis, 2004. Tsunami sources in the southern California bight, Geophys. Res. Lett., 31, L13211, doi:10.1029/2004GL020078.

Borrero, J., Cho, S., Moore, J.E., Richardson, H.W., and C. Synolakis, 2005. Could it happen here? Civil Eng., 75, 54-65.

Burbidge, D., P.R. Cummins, R. Mleczko and H.K. Thio, 2008. Probabilistic tsunami hazard analysis for Western Australia, Pageoph, 165, 2059-2088.

Cisternas, M., B. F. Atwater, F. Torrejo´n, Y. Sawai, G. Machuca, M. Lagos, A. Eipert, C. Youlton, I. Salgado, T. Kamataki, M. Shishikura, C. P. Rajendran, J. K. Malik, Y. Rizal and M. Husni, 2005. Predecessors of the giant 1960 Chile earthquake, Nature 437, 404-407.

Divins, D.L., and D. Metzger, NGDC Coastal Relief Model, Retrieved 10/2007, http://www.ngdc.noaa.gov/mgg/coastal/coastal.html

Earthquake Research Committee (ERC), 2005. National Seismic Hazard Maps for Japan (2005),158 pp.,

Frohlich, Cliff, and Laura Reiser Wetzel (2007), Comparison of seismic moment release rates along different types of plate boundaries, Geophys J Int, 171(2), 909.

Geist, E.L., and Parsons, T., 2006, Probabilistic analysis of tsunami hazards: Natural Hazards, v. 37, p. 277-314

Gica, E., M.H. Teng, P.L.-F. Liu, V. Titov, and H. Zhou, 2007. Sensitivity Analysis of Source Parameters for Earthquake-Generated Distant Tsunamis, J. Waterway, Port, Coastal, Ocean Eng. ASCE, doi: 10.1061/(ASCE)0733-950X(2007)133:6(429).

Hyndman, 2007. The seismogenic zone of subduction thrusts faults, in The seismogenic zone of subduction thrust faults, Dixon, T.H. and J.C. Moore, eds., 15-40.

Jankaew, K., B. F. Atwater, Y. Sawai, M. Choowong, T. Charoentitirat, M. E. Martin and A. Prendergast, 2008. Medieval forewarning of the 2004 Indian Ocean tsunami in Thailand, Nature 455, 1228-1231.

Locat, J., H.J. Lee, P. Locat and J. Imran, 2004. Numerical analysis of the mobility of the Palos Verdes debris avalanche in California, and its implication for the generation of tsunamis. Marine Geol., 203, 269-280.

McCaffrey, R., 1997. Statistical significance of the seismic coupling coefficient, Bull. Seismol. Soc. Am., 87, 1069-1073.

McCaffrey, R., 2008. Global frequency of magnitude 9 earthquakes, Geology, 36, 263-266.

Nanayama, F., K. Satake, R. Furukawa, K. Shimokawa, B.F Atwater, K. Shigeno, and S. Yamaki, 2003. Unusually large earthquakes inferred from tsunami deposits along the Kuril trench, Nature, 424, 660-663.

National Oceanic and Atmospheric Administration (NOAA), National Geophysical Data Center, 2006. 2-minute Gridded Global Relief Data (ETOPO2v2)

Nishenko, S.P. (1985). Seismic potential for large interplate earthquakes along the Chilean and southern Peruvian margins of South America: a quantitative appraisal. Journal of Geophysical Research 90, 3589-3615.

Okal, E.A., J.C. Borrero, and C.E. Synolakis, 2006. Evaluation of Tsunami Risk from Regional Earthquakes at Pisco, Peru, Bull. Seismol. Soc. of Am. 96, 1634-1648.

Okal, E.A., and C.E. Synolakis, 2003. Theoretical comparison of tsunamis from dislocations and landslides, Pure Appl. Geophys., 160, 2177-2188.

Pacheco, J. F., L. R. Sykes, and C. H. Scholz, 1993. Nature of Seismic Coupling Along Simple Plate Boundaries of the Subduction Type, J. Geophys. Res., 98(B8), 14,133–14,159.

Pinegina, T.K., Bourgeois, J., Bazanova, L.I. et al. 2003. A millennial-scale record of Holocene tsunamis on the Kronotskiy bay coast, Kamchatka, Russia. Quaternary Research 59: 36-47.

Satake, K., 1995. Linear and Nonlinear Computations of the 1992 Nicaragua earthquake tsunami, PAGEOH, 144, 455-470.

Satake, Kenji, and Brian F. Atwater, 2007. Long-Term Perspectives on Giant Earthquakes and Tsunamis at Subduction Zones, Ann. Rev Earth Planet Sci, 35(1), 349.

Satake, K., K. Shimazaki, Y. Tsuji and K. Ueda, 1996. Time and size of a giant earthquake in Cascadia inferred from Japanese tsuanmi records of January 1700, Nature, 379, 246-249.

Sawai, Y., Kamataki, T., Shishikura, M., Nasu, H., Okamura, Y., Satake, K., Thomson, K.H., Matsumoto, D., Fujii, Y., Komatsubara, J., Aung, T.T. (2008): Aperiodic recurrence of geologically recorded tsunamis during the past 5500 years in eastern Hokkaido , Japan . Journal of Geophysical Research, doi:10.1029/2007JB005503.

Scholz, C. H., and J. Campos (1995), On the mechanism of seismic decoupling and back arc spreading at subduction zones, J. Geophys. Res., 100(B11), 22,103–22,115.

Schwarz, S., 1999. Noncharacteristic behavior and complex recurrence of large subduction zone earthquakes, J. Geophys. Res., 204, 23,111-23,125.

Shennan, I., Gruhn, R. and G. Plafker, 2009. Multi-segment earthquakes and tsunami potential of the Aleutian megathrust, Quat. Sc. Rev., 28, 7-13.

Sieh, K., Natawidjaja, D. H., Meltzner, A. J., Shen, C.-C., Cheng, H., Li, K.-S., Suwargadi, B. W., Galetzka, J., Philibosian, B., and Edwards, R. L., 2008. Earthquake Supercycles Inferred from Sea-Level Changes Recorded in the Corals of West Sumatra, Science 322, 1674-1678, doi: 10.1126/science.1163589.

Stein, S. and E. Okal, 2007. Ultralong period seismic study of the December 2004 Indian Ocean earthquake and implications for regional tectonics and the subduction process, Bull. Seismol. Seoc. Am., 97, S279-S295.

Suarez, G., A., Paola, 2009. Evidence for Great Tsunamigenic Earthquakes (M 8.6) along the Mexican Subduction Zone, Bull. Seismol. Soc. Am. 99, 892-896.

Taylor, L.A., B.W. Eakins, K.S. Carignan, R.R. Warnken, D.C. Schoolcraft, G.F. Sharman, 2008. Digital Elevation Model Of Port San Luis, California: Procedures, Data Sources And Analysis, NOAA Technical Memorandum NESDIS NGDC-3.

Taylor, L.A., B.W. Eakins, K.S. Carignan, R.R. Warnken, T. Sazonova, and D.C. Schoolcraft, 2008. Digital Elevation Model for Monterey, California: Procedures, Data Sources and Analysis, Prepared for the Pacific Marine Environmental Laboratory (PMEL) NOAA Center for Tsunami Research by the NOAA National Geophysical Data Center (NGDC).

Thatcher, W. (1990), Order and Diversity in the Modes of Circum-Pacific Earthquake Recurrence, J. Geophys. Res., 95(B3), 2609–2623.

Thio, H.K., P. Somerville and Gene Ichinose (2007). Probabilistic Analysis of Strong Ground Motion and Tsunami Hazards in Southeast Asia. Journal of Earthquake and Tsunami, 1, No. 2., p. 119-137.

Titov, V.V., and C.E. Synolakis, 1996. Numerical modeling of 3-D long wave run-up using VTCS-3. In Long Wave Run-up Models, P. Liu, H. Yeh, and C. Synolakis (eds.), World Scientific Publishing Co. Pte. Ltd., Singapore, 242–248.

Titov, V.V. and F. Gonzalez, 1997. Implementation and testing of the method of splitting tsunami (MOST) model, NOAA Technical Memorandum ERL PMEL-112.

Wang, R, F. Lorenzo-Martín and F. Roth, 2003. Computation of deformation induced by earthquakes in a multi-layered elastic crust—FORTRAN programs EDGRN/EDCMP, Computers & Geosciences, 29, 195–207.

Wang, R, F. Lorenzo-Martín and F. Roth, 2006. Erratum to: "Computation of deformation induced by earthquakes in a multi-layered elastic crust—FORTRAN programs EDGRN/EDCMP", Computers & Geosciences, 32, 1817.

Watts, P., 2004, Probabilistic predictions of landslide tsunamis off southern California: Marine Geology, v. 203, p. 281-301.

11. TABLES

Table 1 Grids used in the finite difference computations

Grid #	Cell-size (arcsec)	Longitude range	Latitude range	Provenance
0	120	120.0 – -70.0	-58.0 – 62.0	ETOPO2v2
1	24	-136.0 - -116.0	31.0 – 43.0	NOAA
2	4.8	-124.5 - -124.0	40.2 – 42.5	NOAA/CICORE
3	4.8	-124.2 - -123.6	38.7 – 40.0	NOAA
4	4.8	-123.2 - -122.0	37.1 – 38.4	NOAA
5	4.8	-122.5 - -121.6	36.1 – 37.0	USGS
6	4.8	-121.5 - -120.3	34.6 – 35.9	NOAA-TGP
7	4.8	-120.2 - -119.0	33.8 – 34.5	NOAA-TGP
8	4.8	-118.9 - -117.0	32.5 - 34.1	NOAA

Table 2 Recurrence parameters for major subduction zone earthquakes

Subduction zone	Convergence rate (McCafrey)	M_{max} predicted	M_{max} obs
Alaska – Aleutian[1]	18-76	9.5	9.3
Kamchatka-Kuriles[2]	69-84	9.1	9.0
Izu-Bonin-Marianas	31-70	9.2	7.2
Ryukyu	74-92	9.2	8.1
Philippines	95-113	9.4	8.0
Solomon	86-105	9.5	8.1
Vanuatu	57-175	9.1	8.1
Chile	63-75	9.5	9.5
Peru	58-70	9.5	9.2

[1] Details in Table 3, [2] details in Table 4

Table 3 Recurrence model for the Alaska - Aleutian subduction zone

Model	Segment	Length	Rate	Mmax	Lon. range	Recur
USGS	All			7-8	-195.0 - -144.0	G-R
	Yakataga			7 – 8.1	-145.5 - -139.5	G-R
	East			9.2	-154.5 - -144.0	Max
	Kodiak			8.8	-154.5 - -149.0	Max
	Semidi			8 – 8.5	-158.0 - -154.0	G-R
	Shumagin			-	-	-
	Western			8-9.2	-190.0 - -163.0	G-R
	Komandorski			8 – 8.2	-195.0 - -190.0	G-R
McCafrey	Alaska	1489	55-66	9.5	--144 - -164	Max
	East Aleutian	1092	64-76	9.3	-164 - -180	Max
	Western Aleutian	1244	69-80	9.3	-180 - --195	Max

Table 4 Recurrence model for the Kamchatka-Kurile subduction zone

	Mmax	ARP
J1 - Japan trench	8.2	72
K1 - Tokachi-oki	7.9	72
K2 - Nemuro-oki	7.8	72
K3 - Shikotanto-oki	8.2	72
K4 - Etorofuto-oki	8.2	72
K5	8.3	*
K6 - “2006”	8.5	*
K7	8.6	*
K8 - “1952”	9.2	*
K9	8.0	*
K10	8.0	*

* - recurrence from convergence rate

12. FIGURES

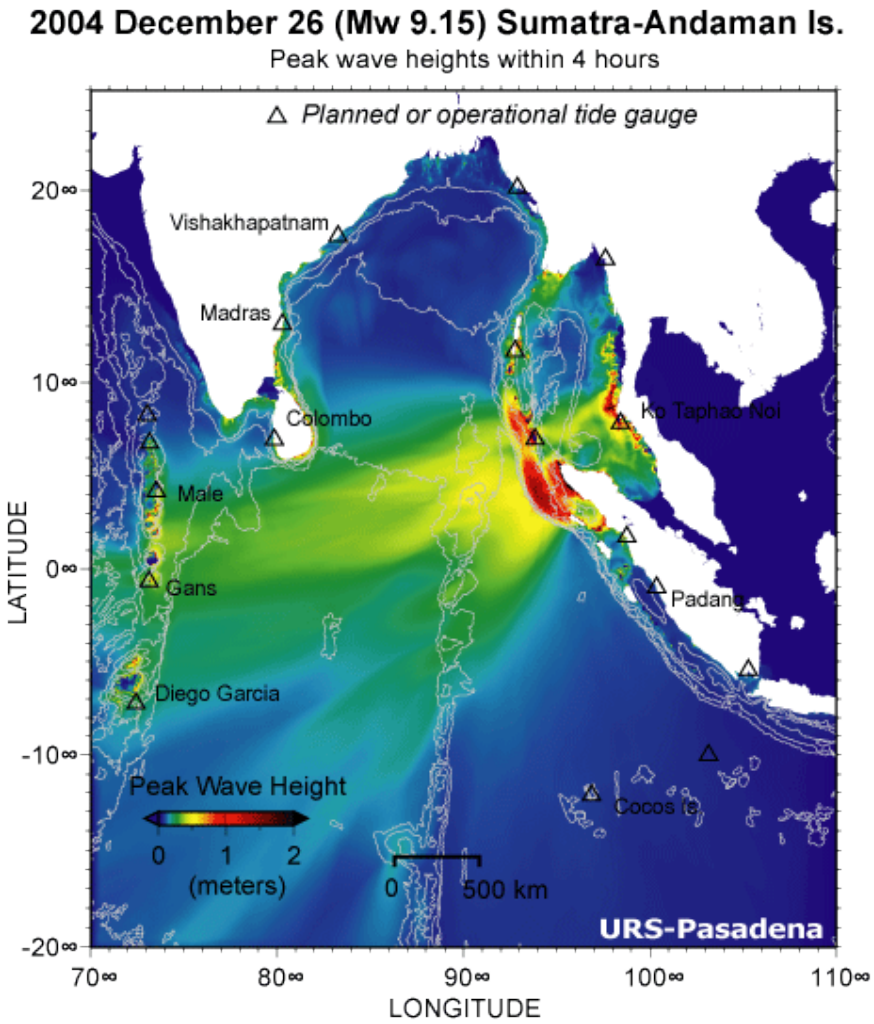

Figure 1 Finite difference calculation of the tsunami wavefield for the 2004 Sumatra earthquake.

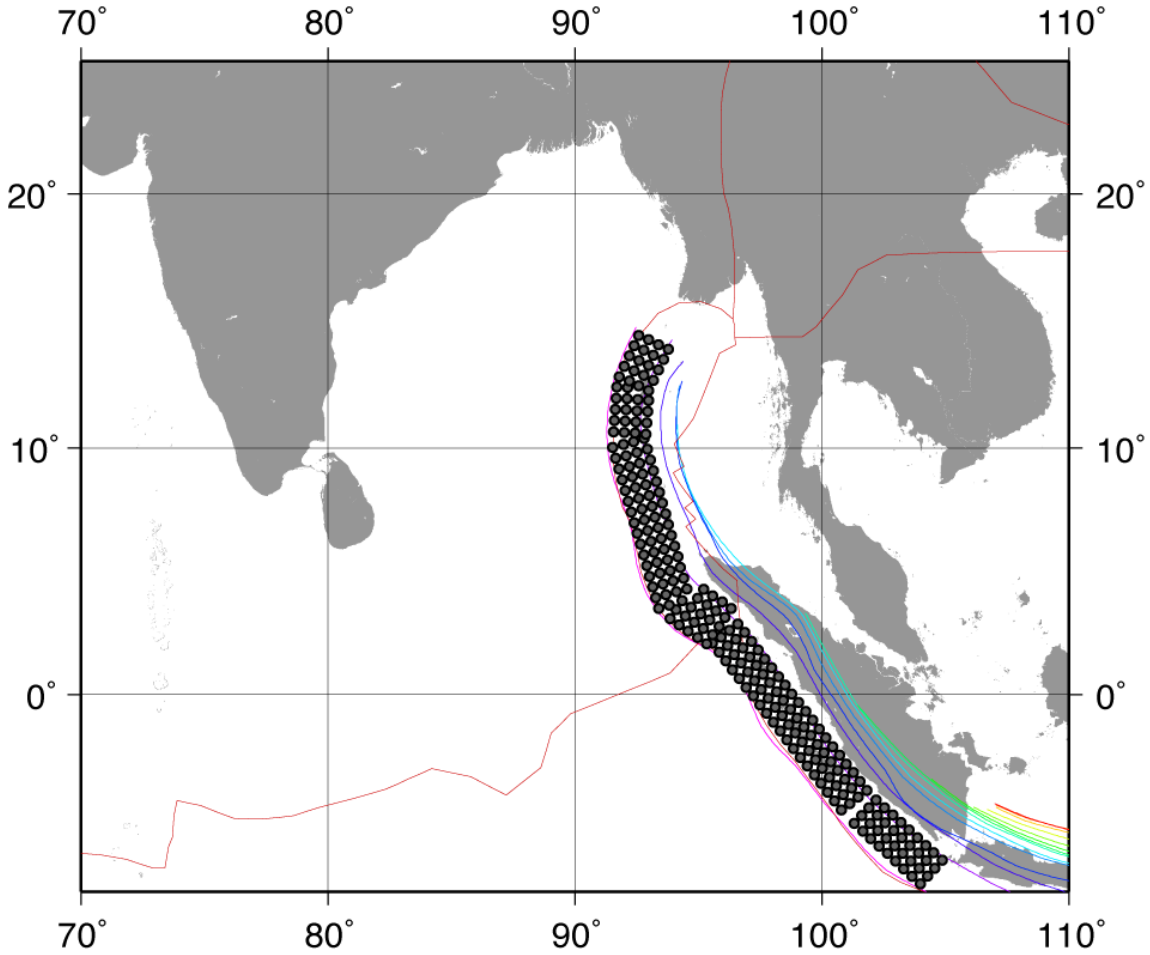

Figure 2 Example of the rupture parameterization using subfaults.

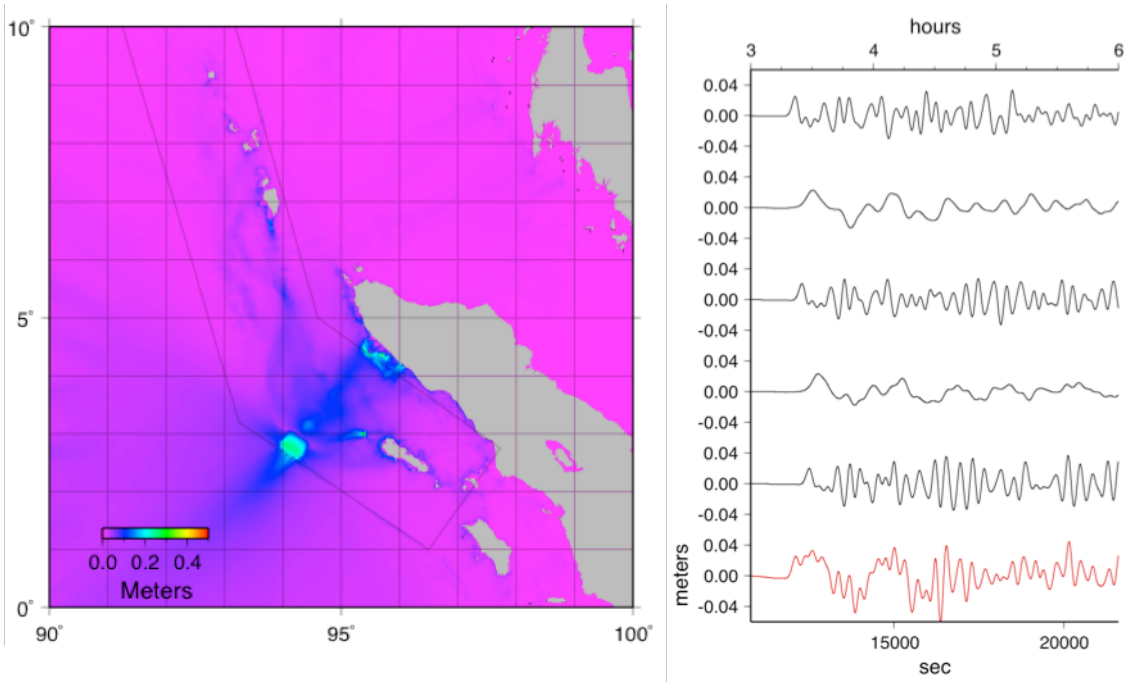

Figure 3 Summation of Green's functions. Wavefield for an individual subfault (left). Summation of several subfault Gren's funtions to compute tsunami response (red line) from a compound rupture.

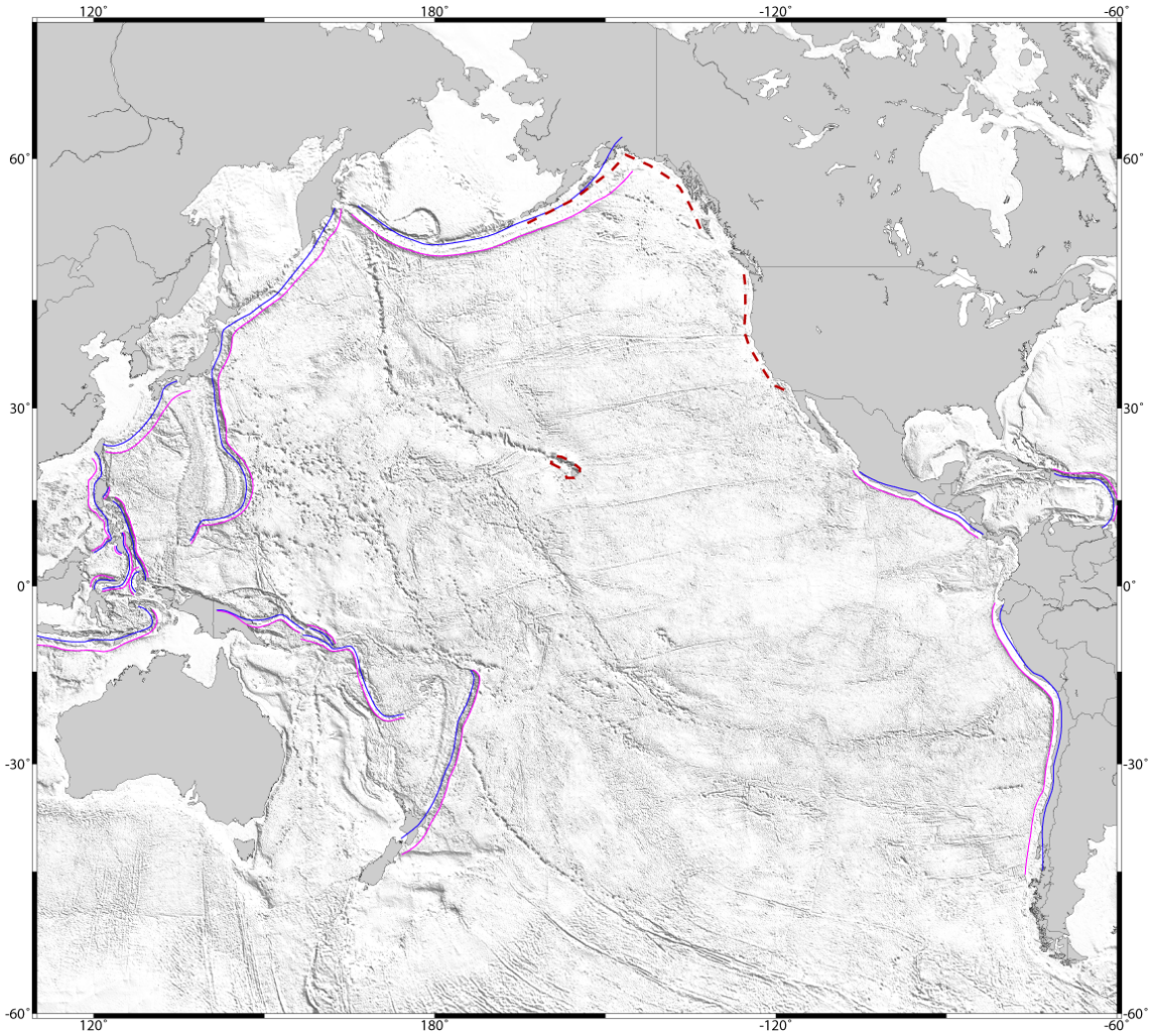

Figure 4 Map of the Pacific Ocean showing the source regions used in this study

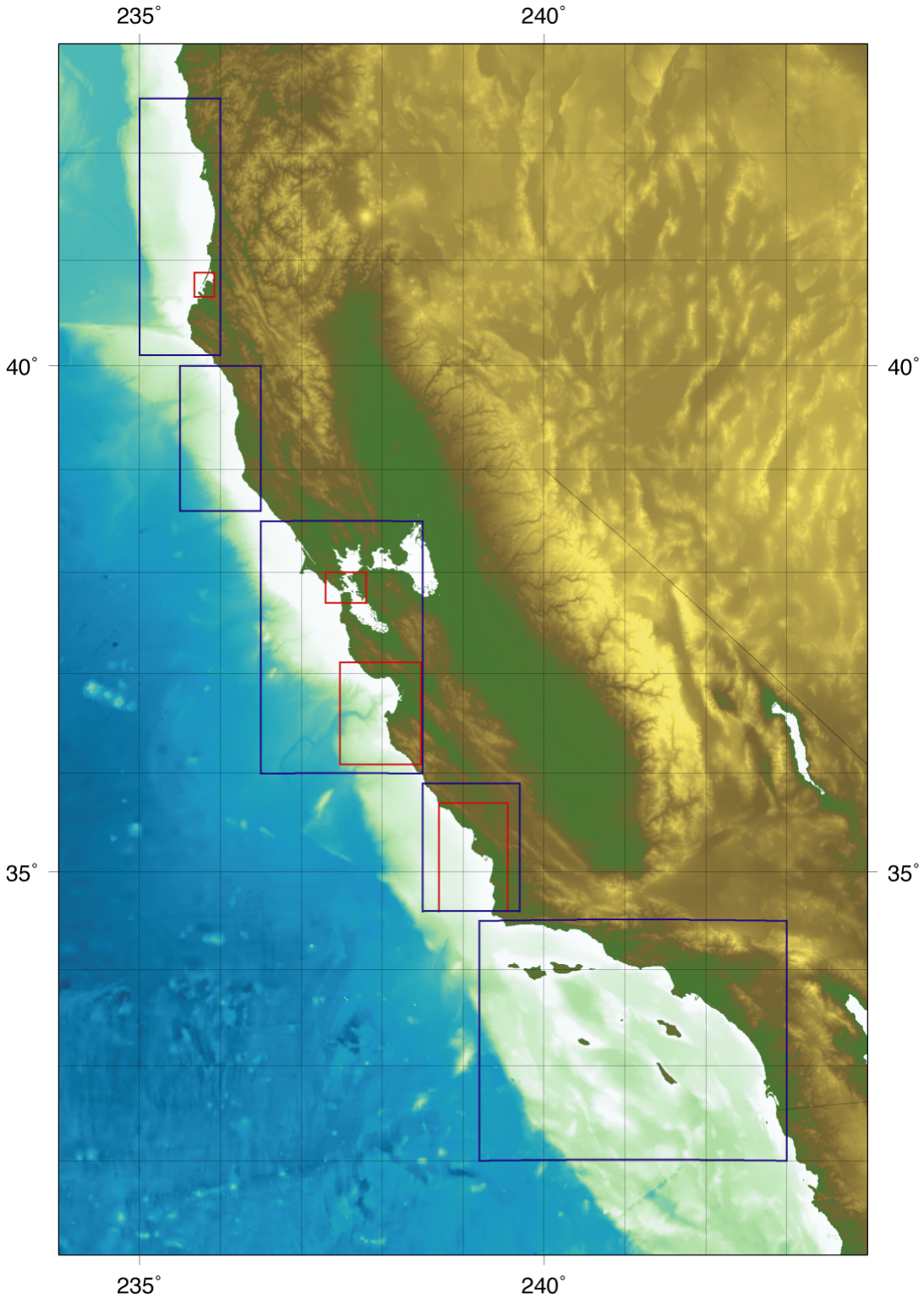

Figure 5 Bathymetric model of California showing the extent of the intermediate (blue boxes) and finest (red boxes) grids.

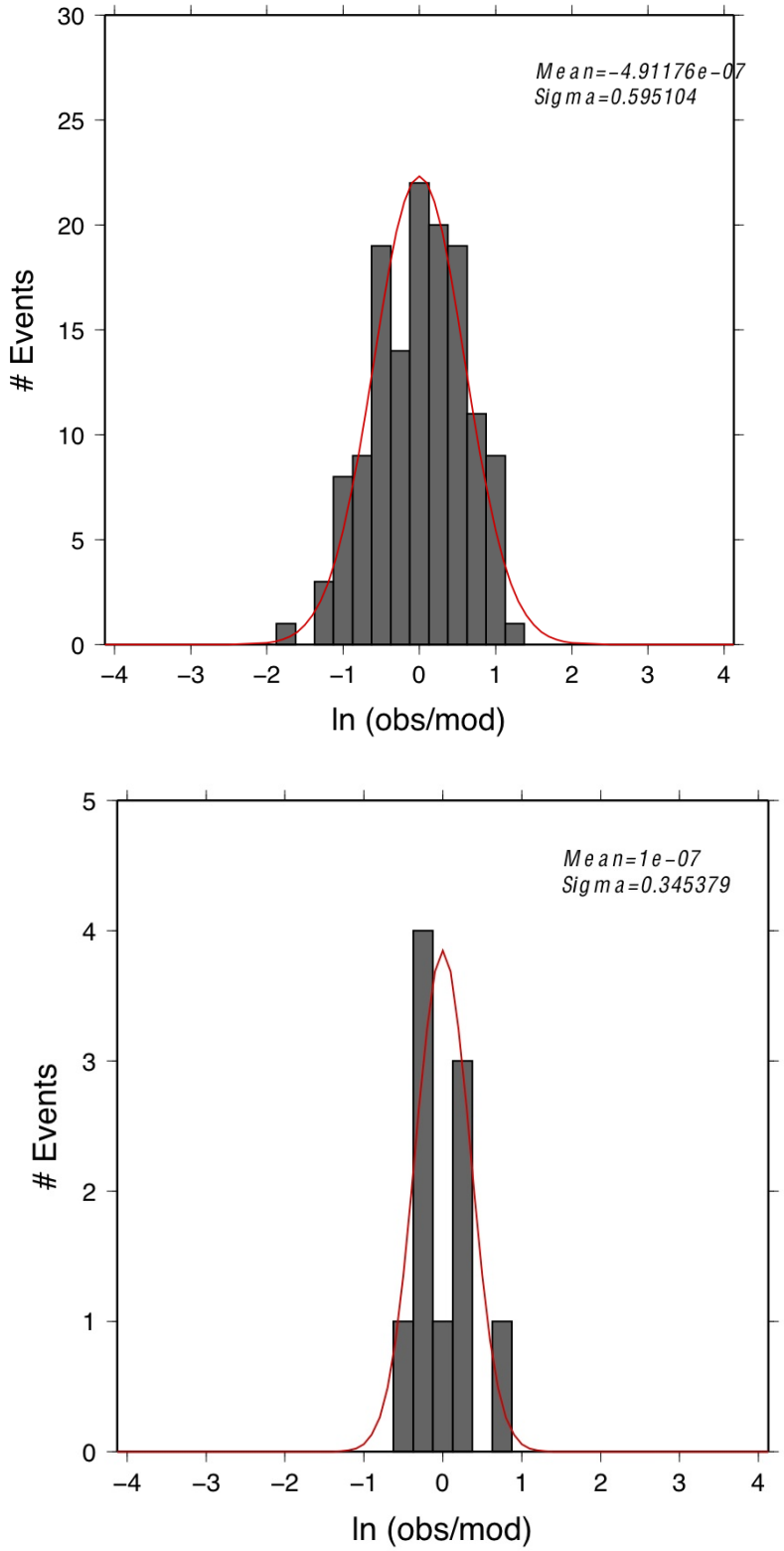

Figure 6 Misfit of tsunami simulation with observed data for a coarse grid (top) and a fine grid (bottom).

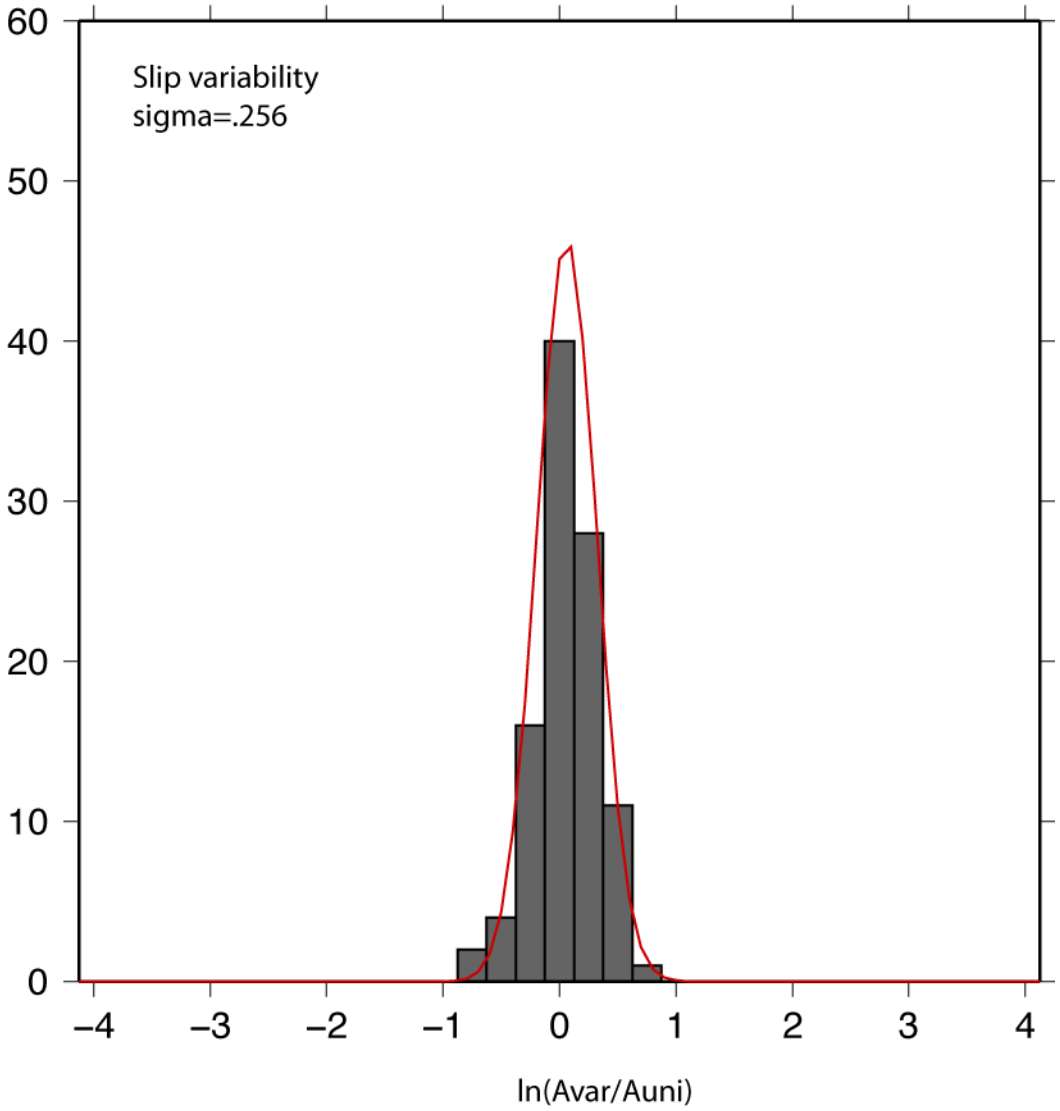

Figure 7 Variability of tsunami amplitudes due to source slip distributions

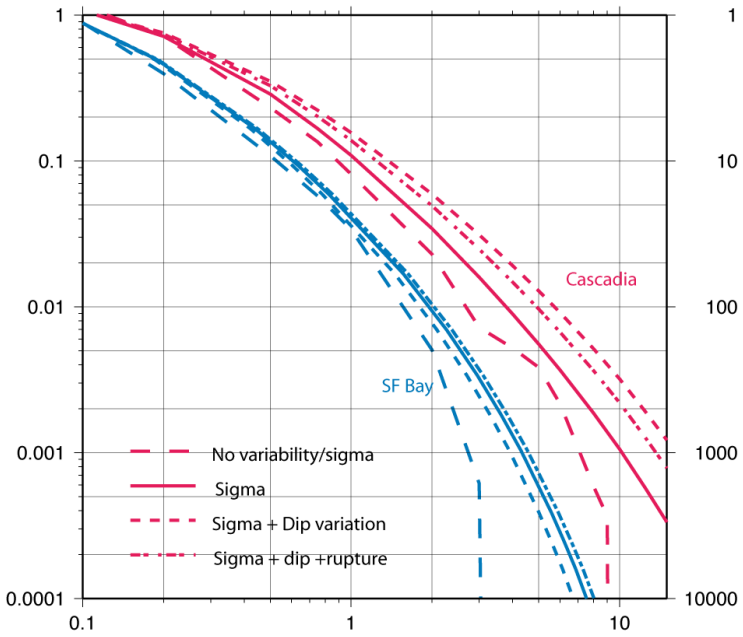

Figure 8 Effect of different sources of uncertainty on the hazard curves at two locations,

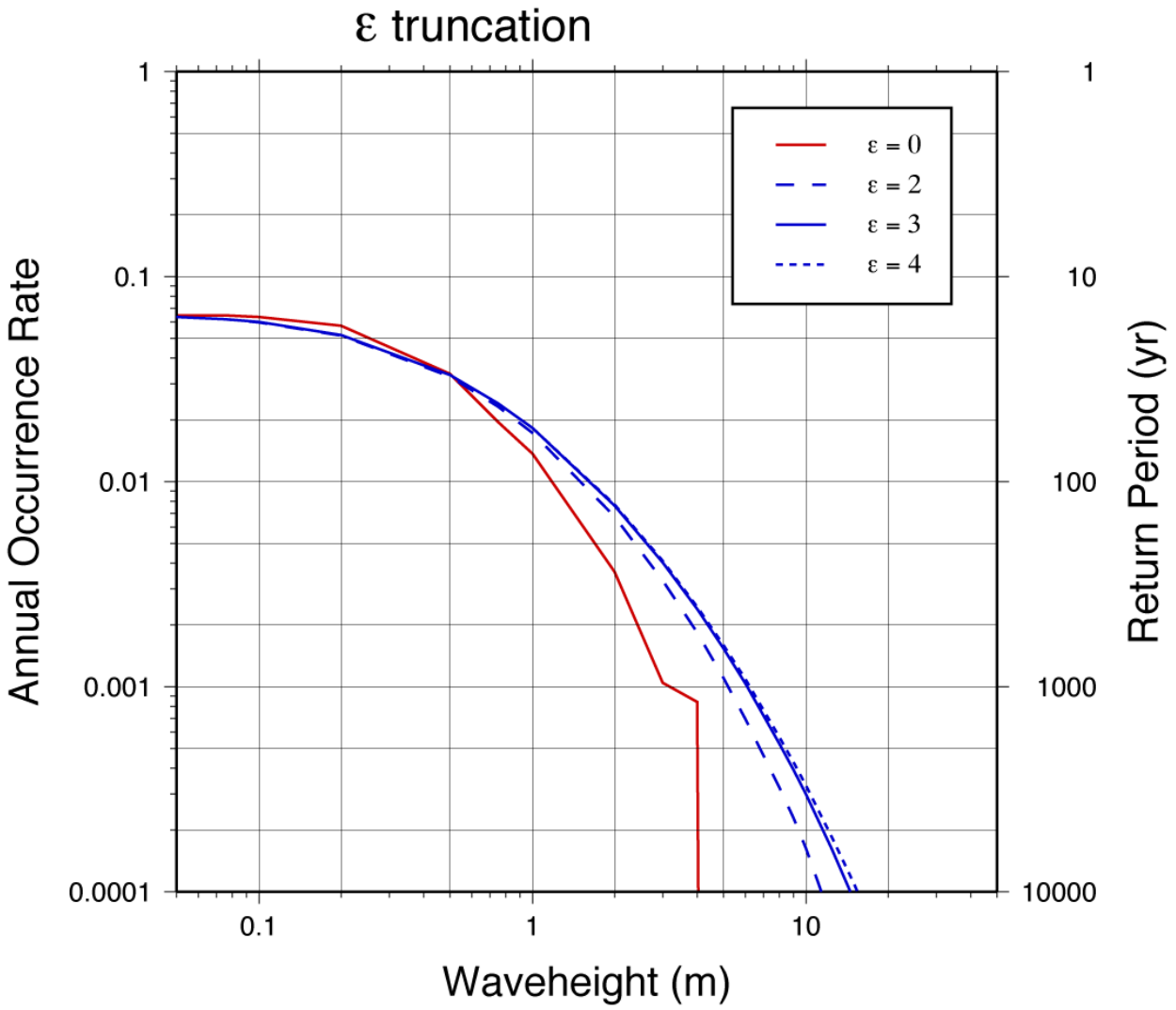

Figure 9 Effect of epsilon truncation on hazard curves.

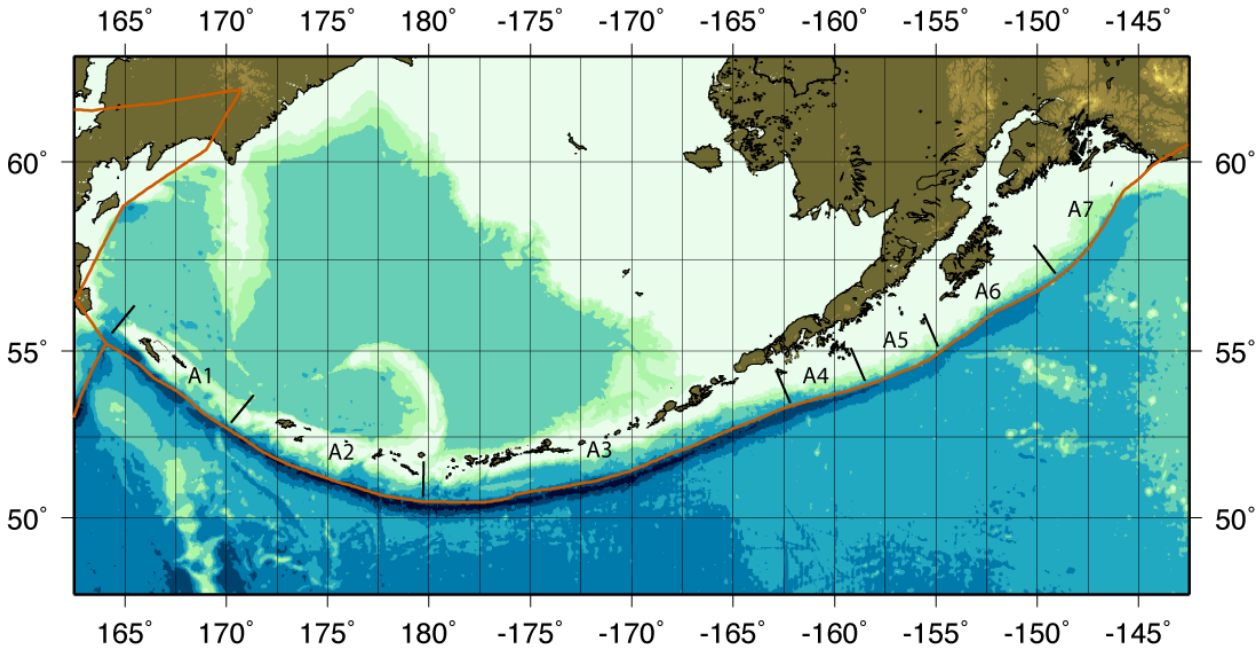

Figure 10 Segmentation model for the Alaska-Aleutian subduction zone.

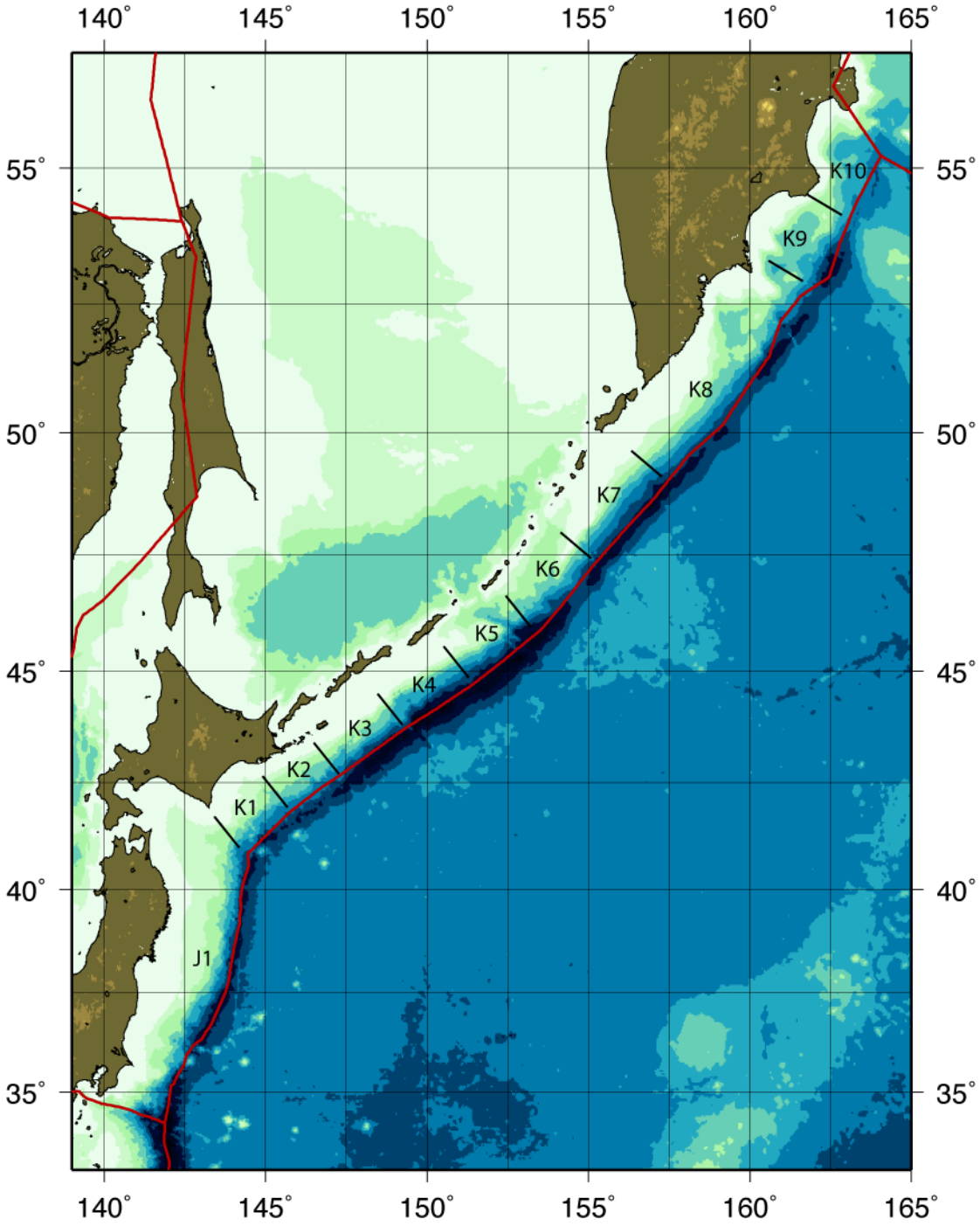

Figure 11 Segmentation model for the Kuril-Kamchatka subduction zone.

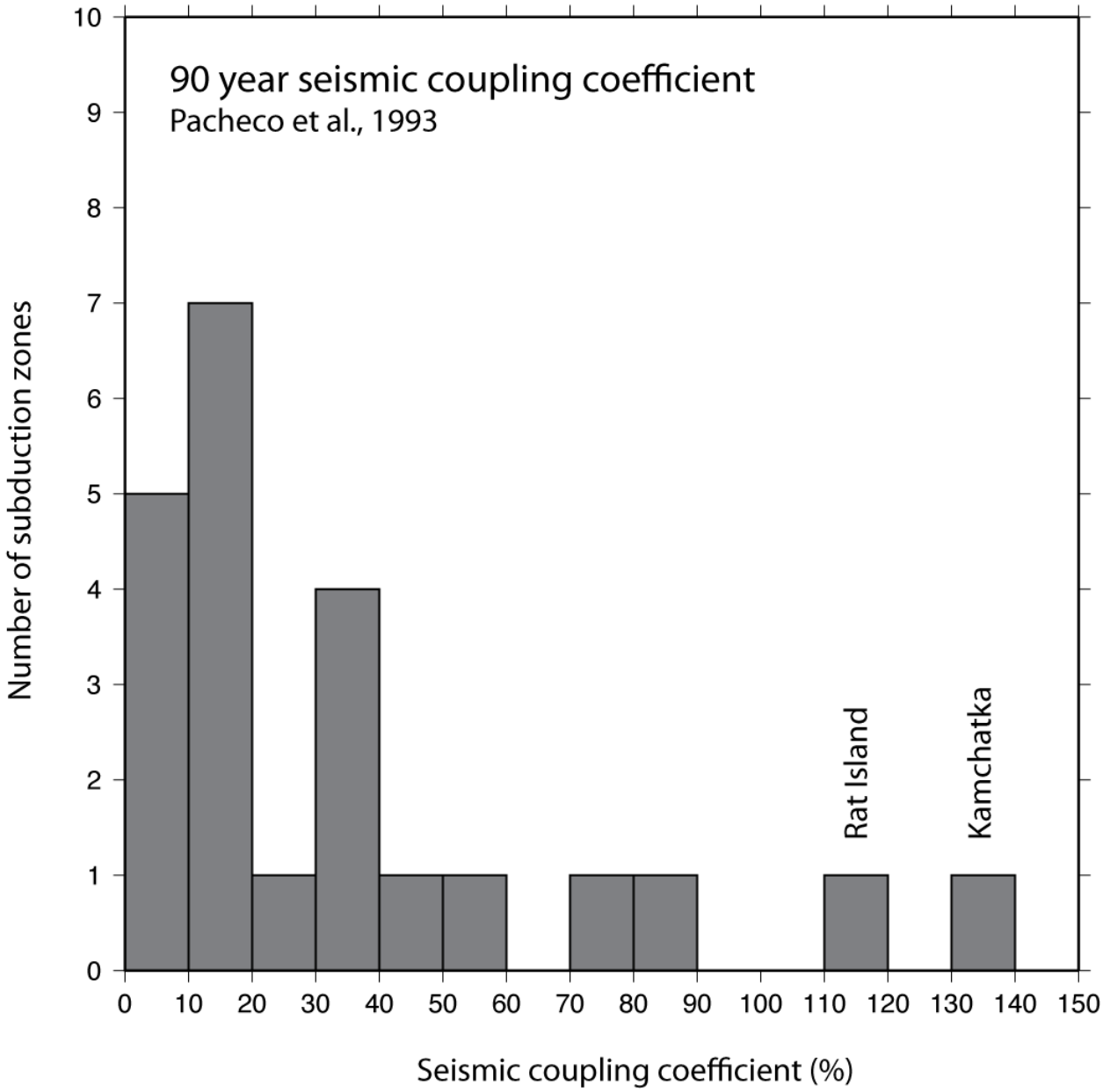

Figure 12 Seismic coupling coefficients.

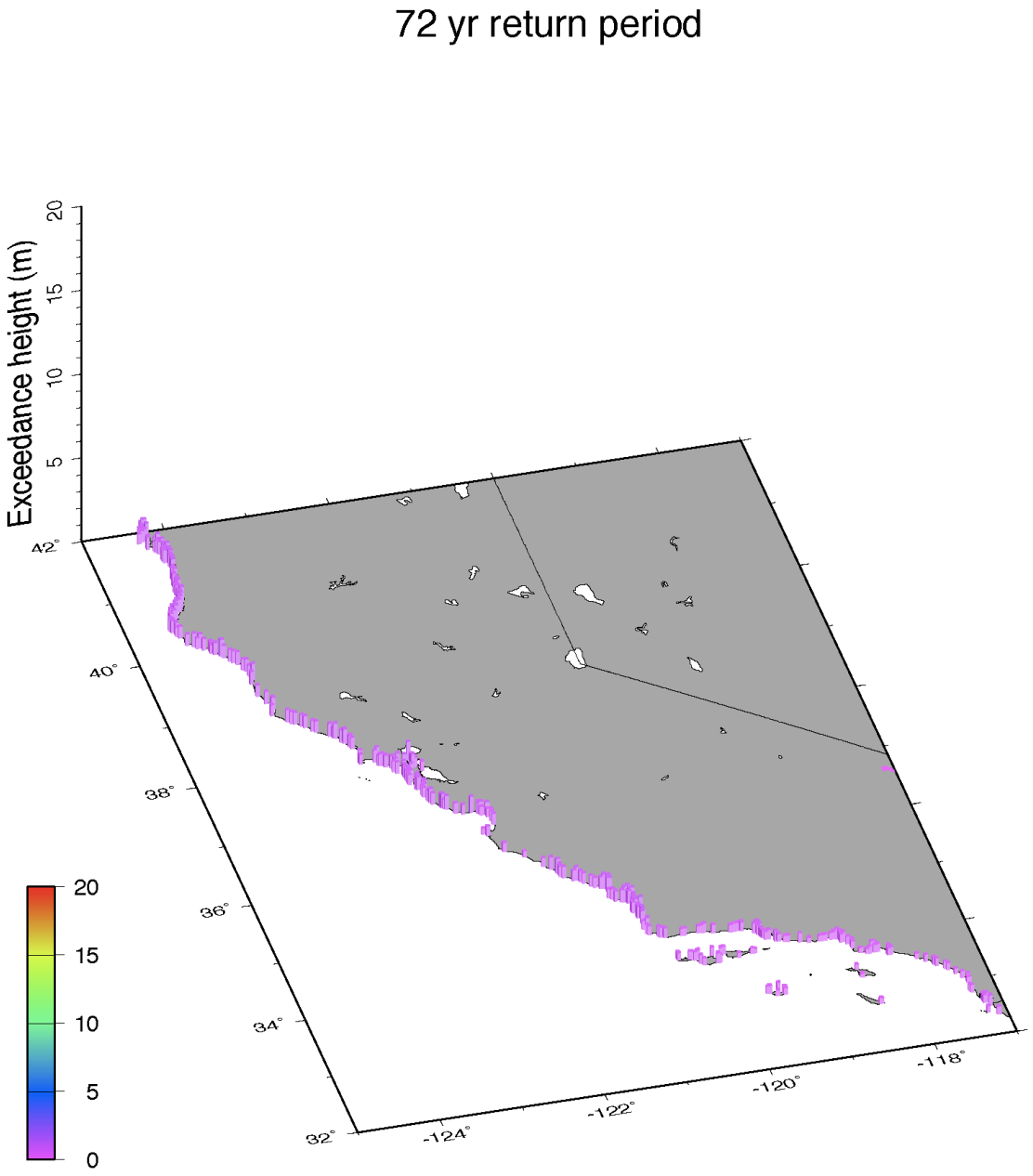

Figure 13 Offshore exceedance waveheight for a 72 yr return period.

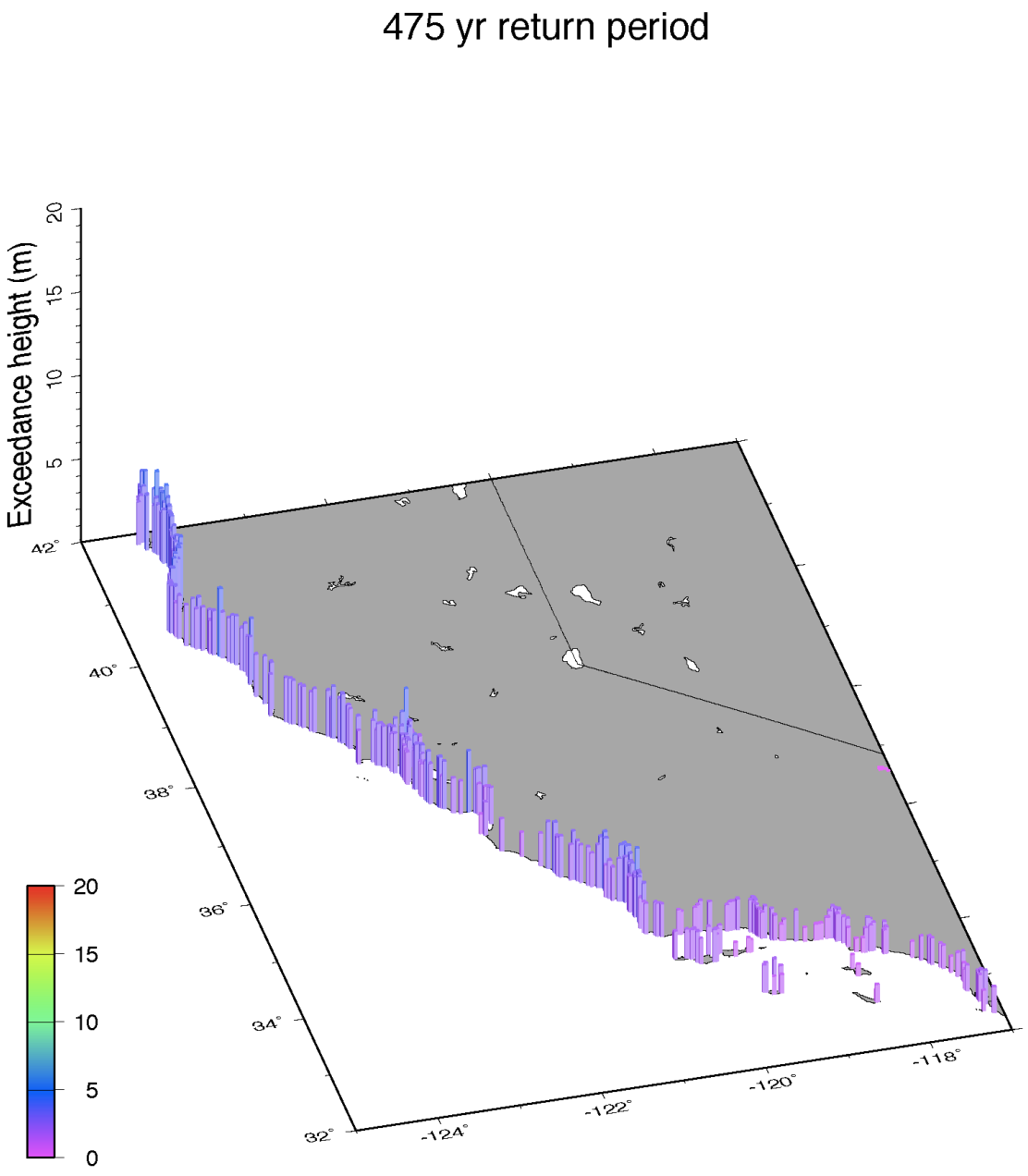

Figure 14 Offshore exceedance waveheights for a 475 yr return period.

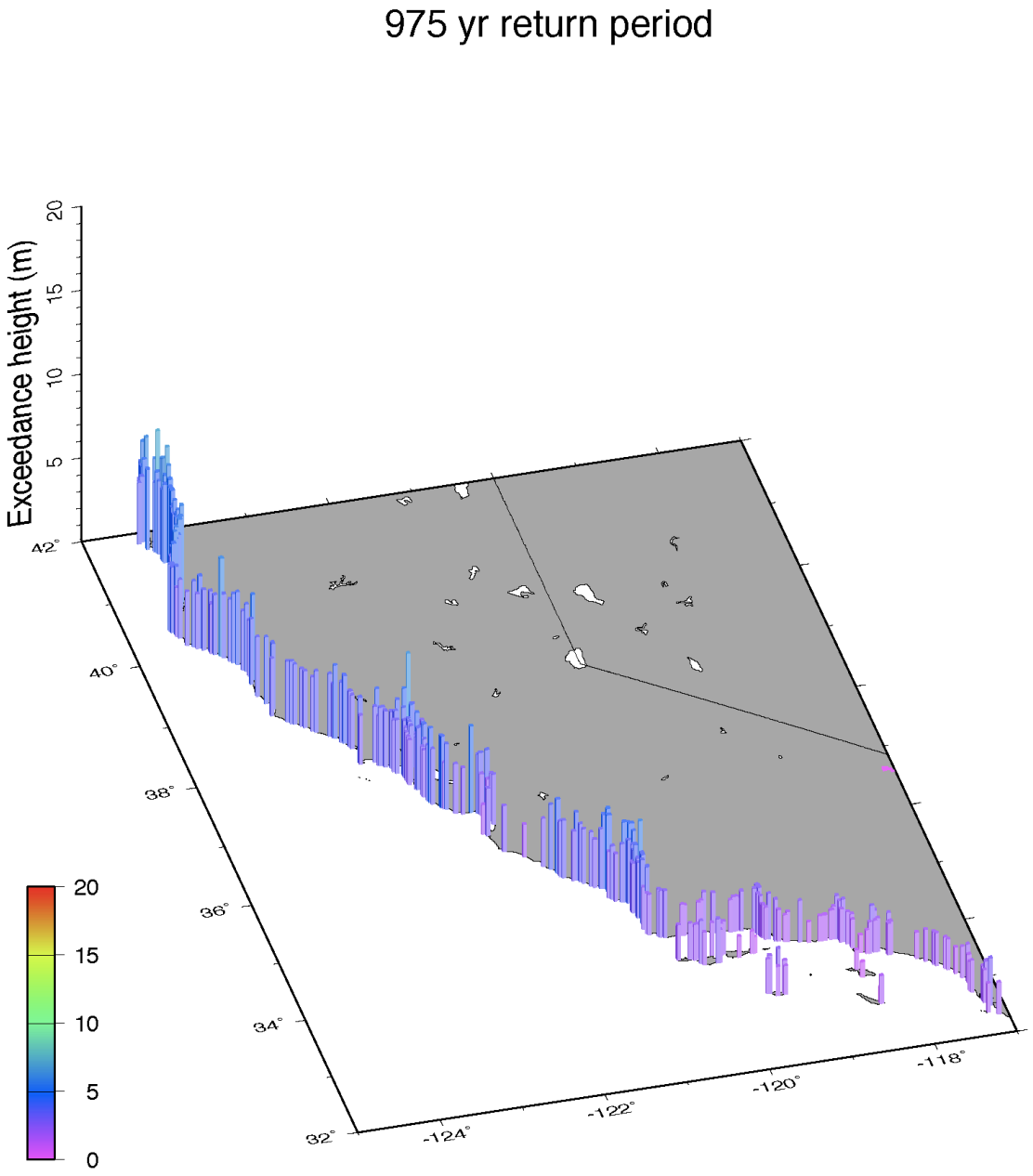

Figure 15 Offshore exceedance waveheight for a 975 yr return period.

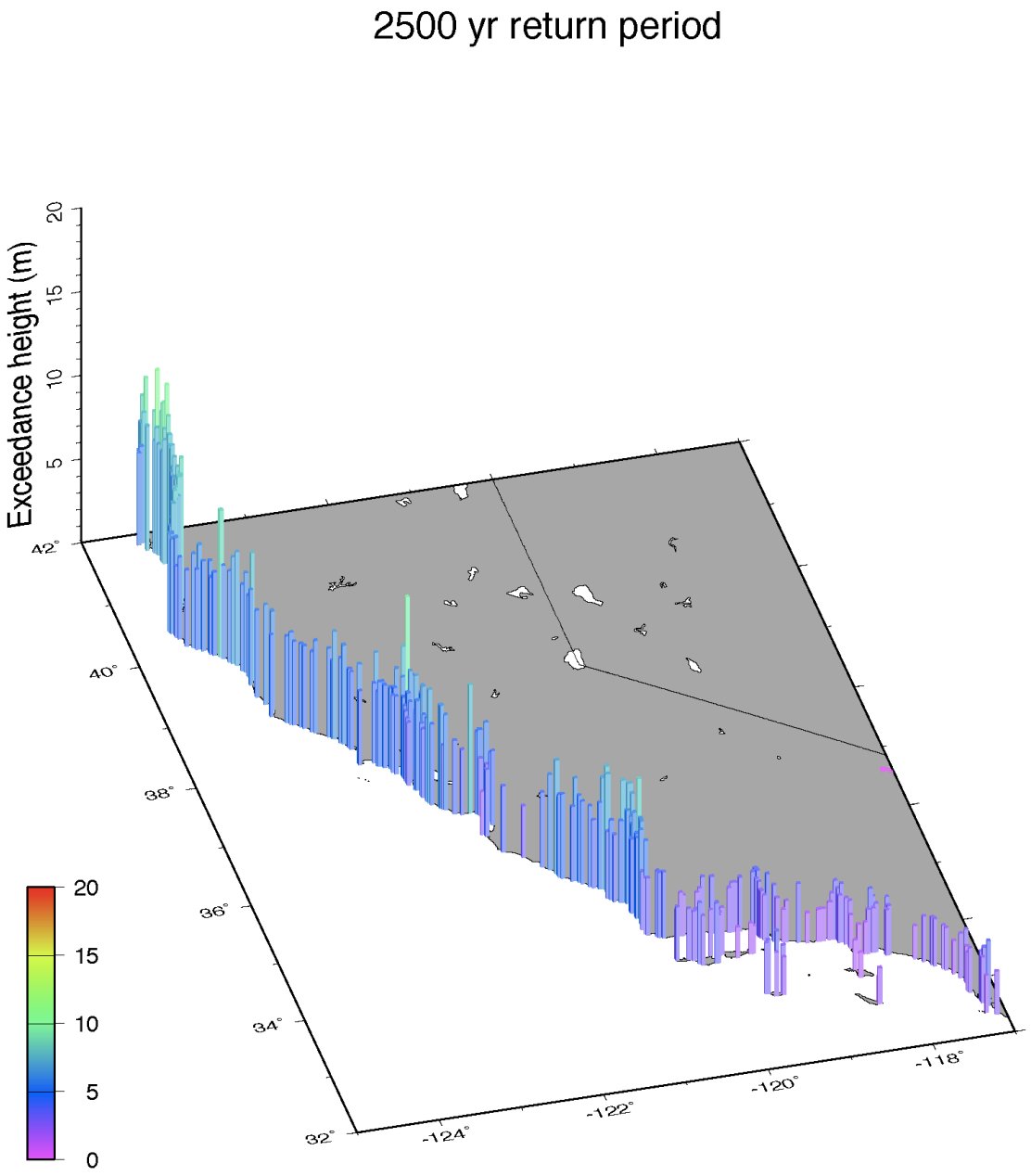

Figure 16 Ofshore exceedance waveheight for a 2500 yr return period.

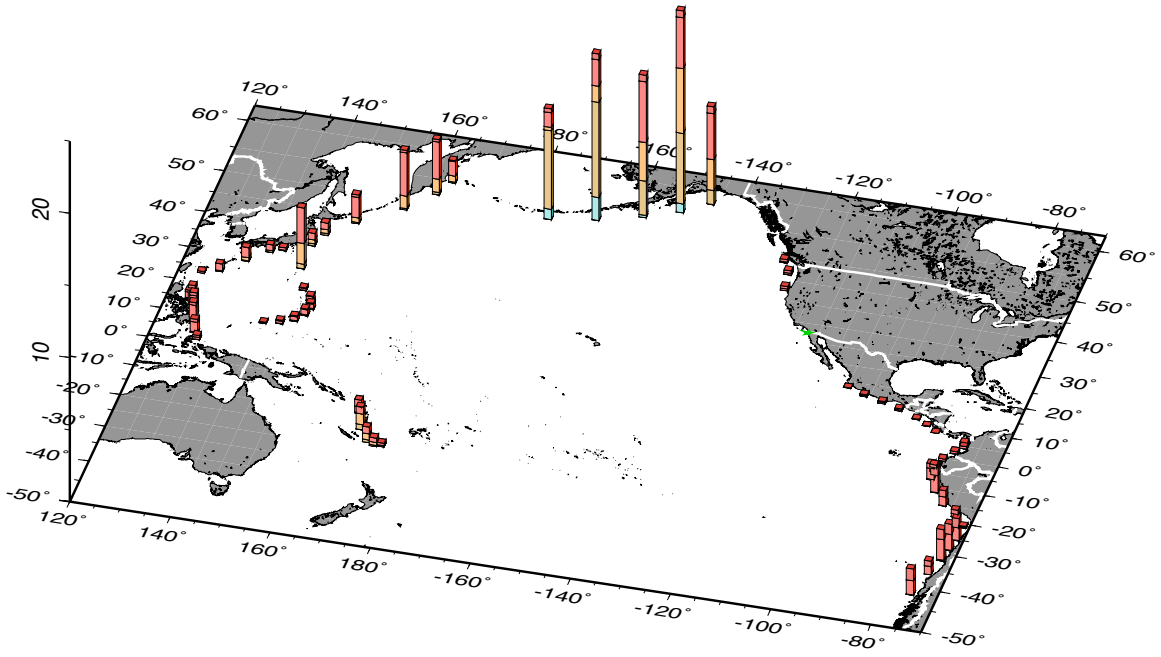

Figure 17 Rupture segment disaggregation for offshore San Diego, 475 yr ARP.

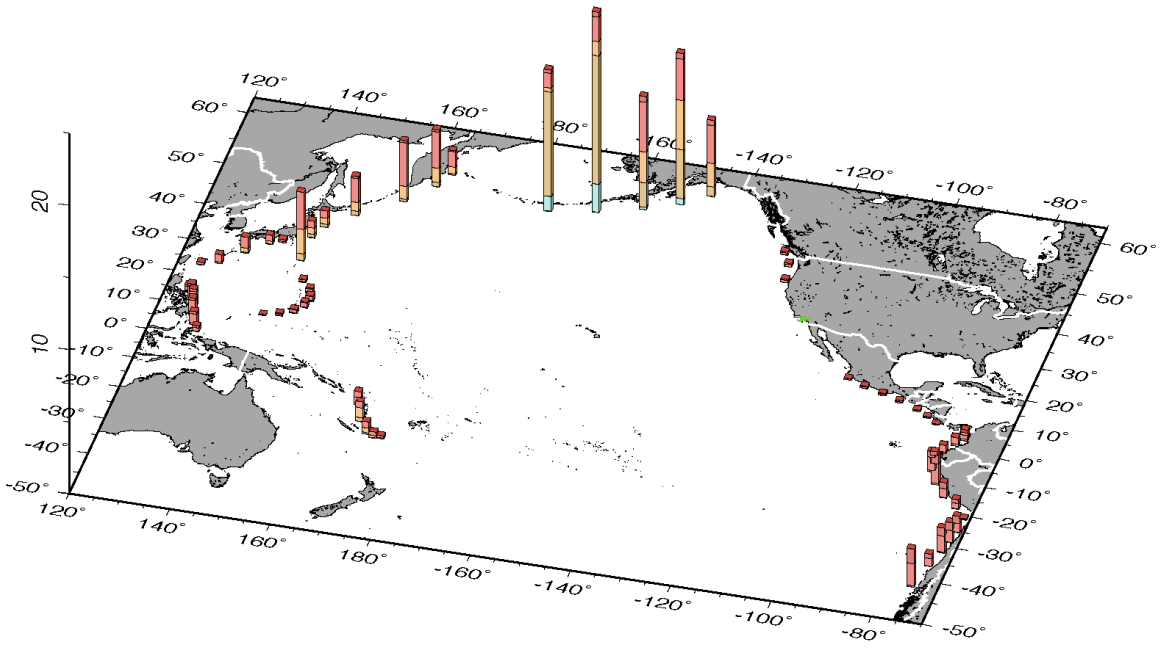

Figure 18 Rupture segment disaggregation for Santa Monica, 475 yr ARP.

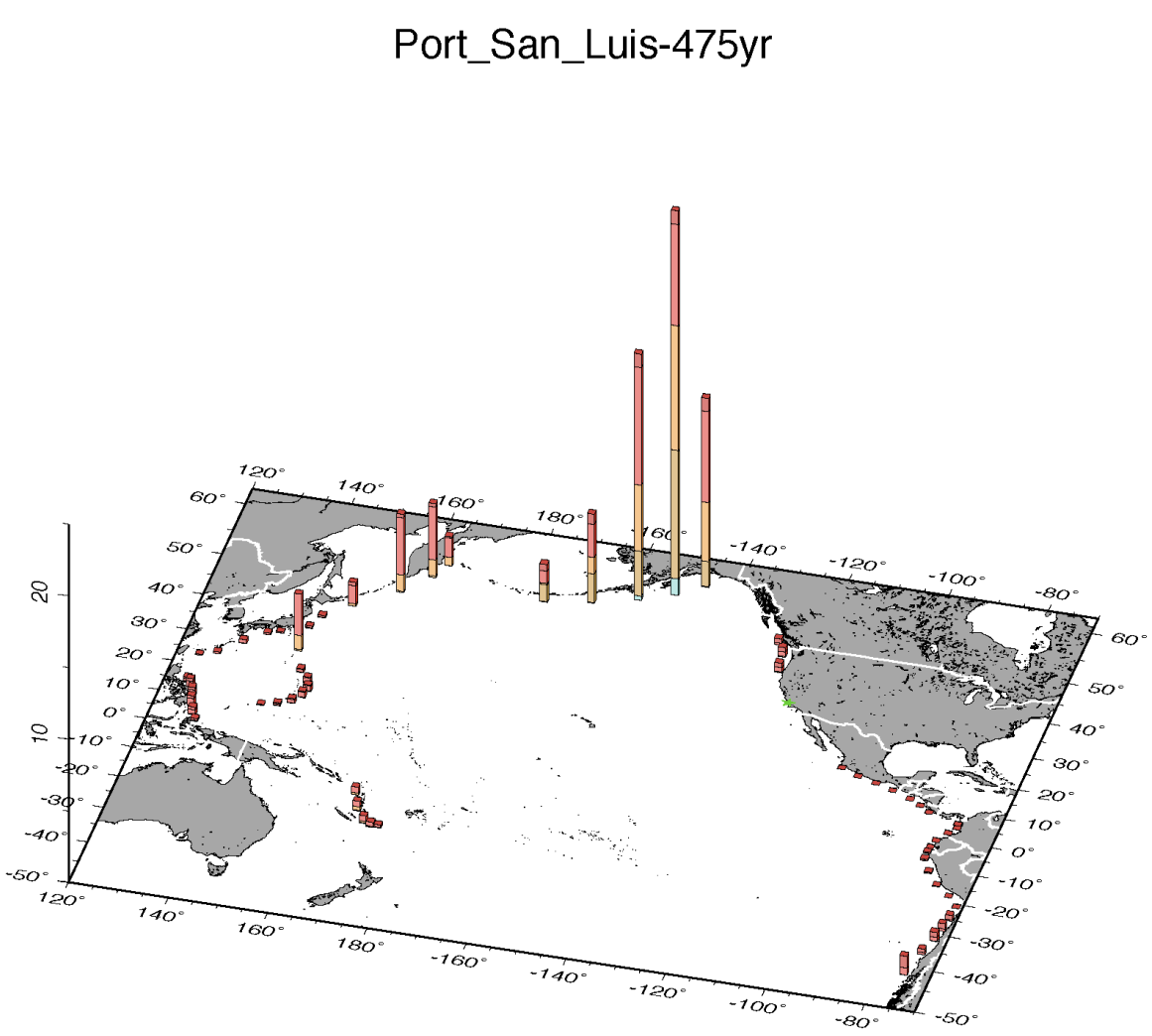

Figure 19 Rupture segment disaggregation for Port San Luis (Avila Beach), 475 yr ARP.

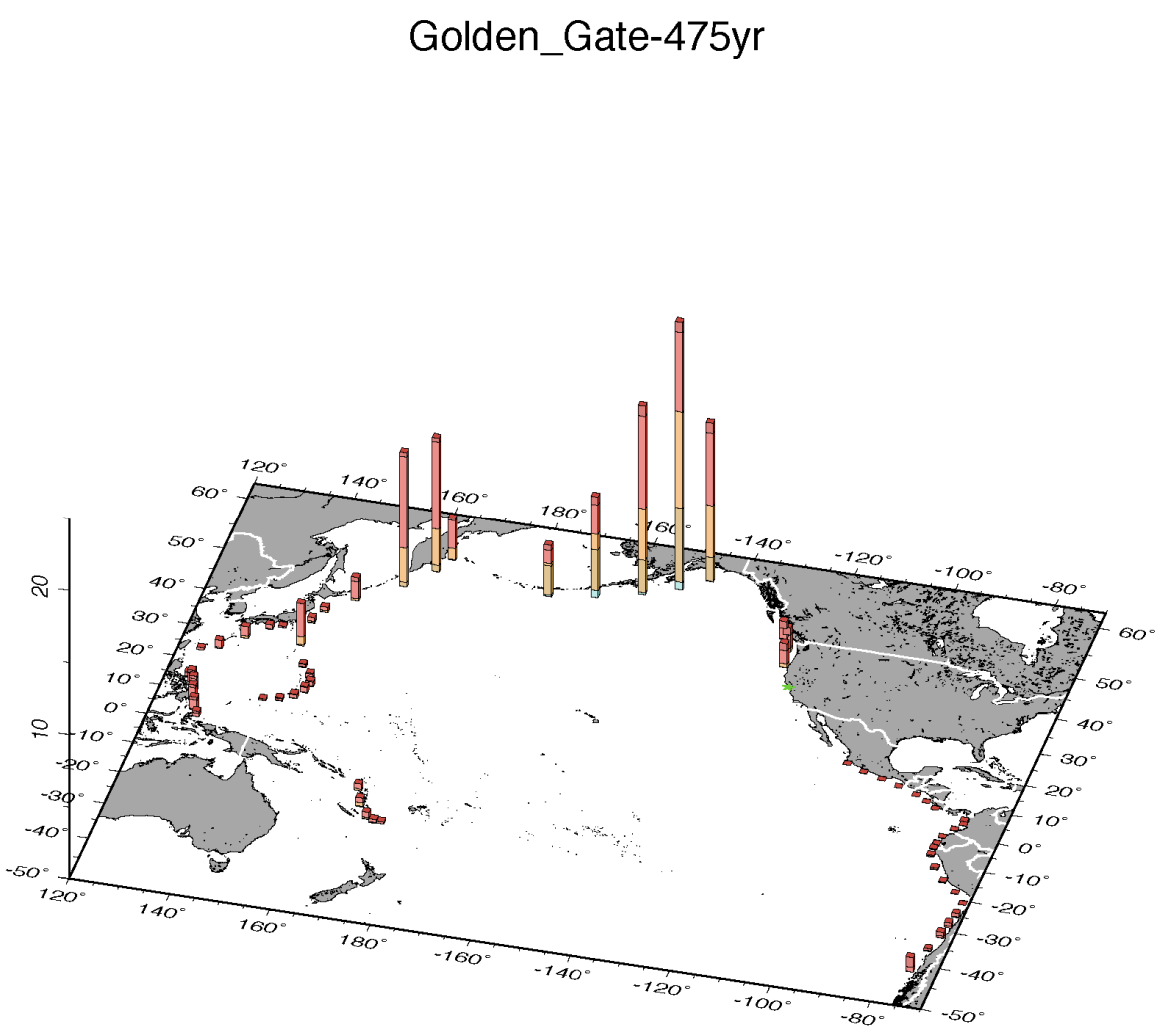

Figure 20 Rupture segment disaggregation for the Golden Gate (offshore, Pacific side), 475 yr ARP.

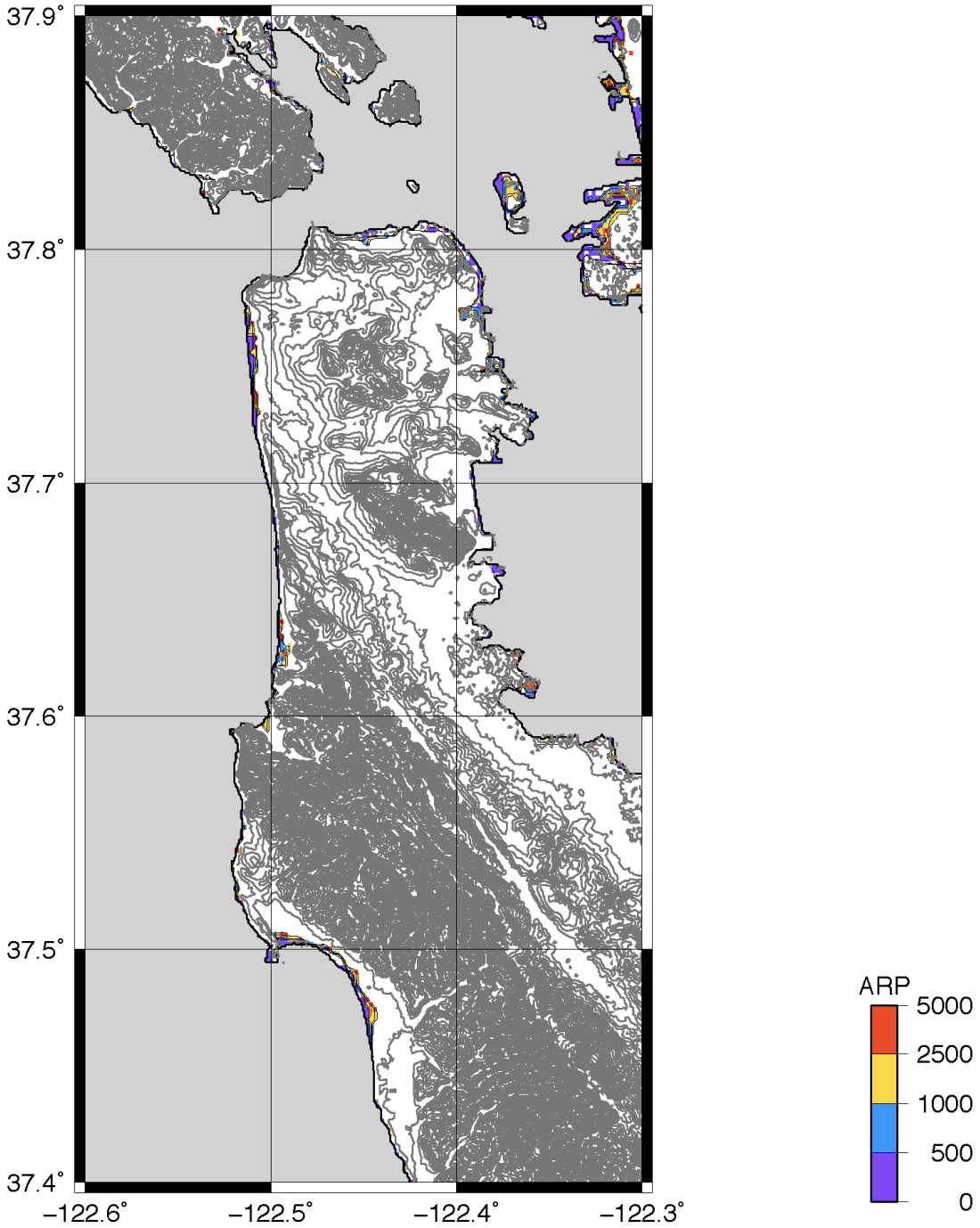

Figure 21 Probabilistic inundation map for the San Francisco Bay area.

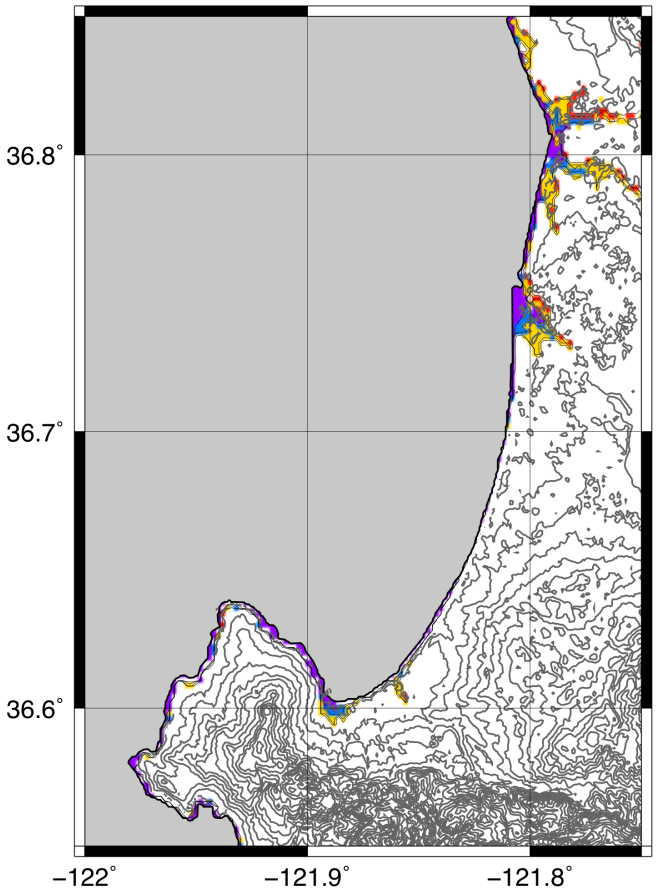

Figure 22 Probabilistic inundation map of southern Monterey Bay

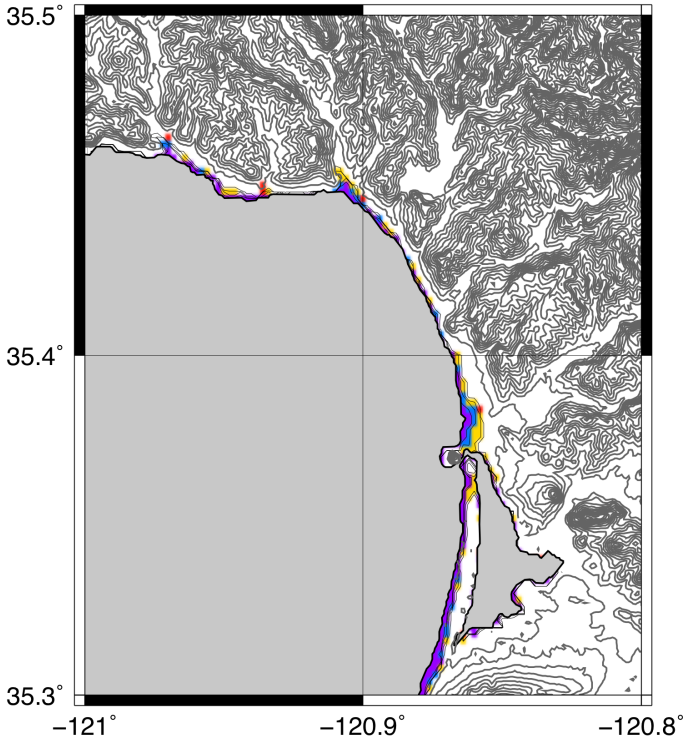

Figure 23 Probabilistic inundation map for Morro Bay.

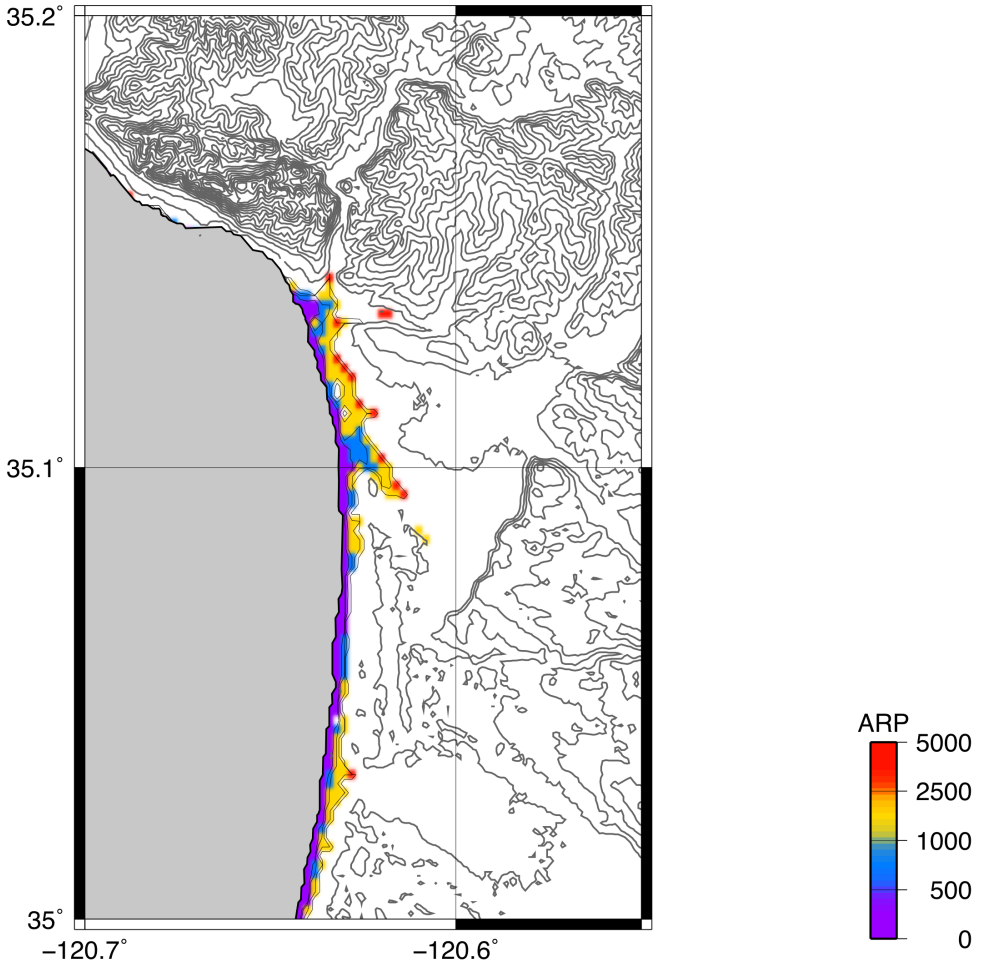

Figure 24 Probabilistic inundation map for Pismo Beach.

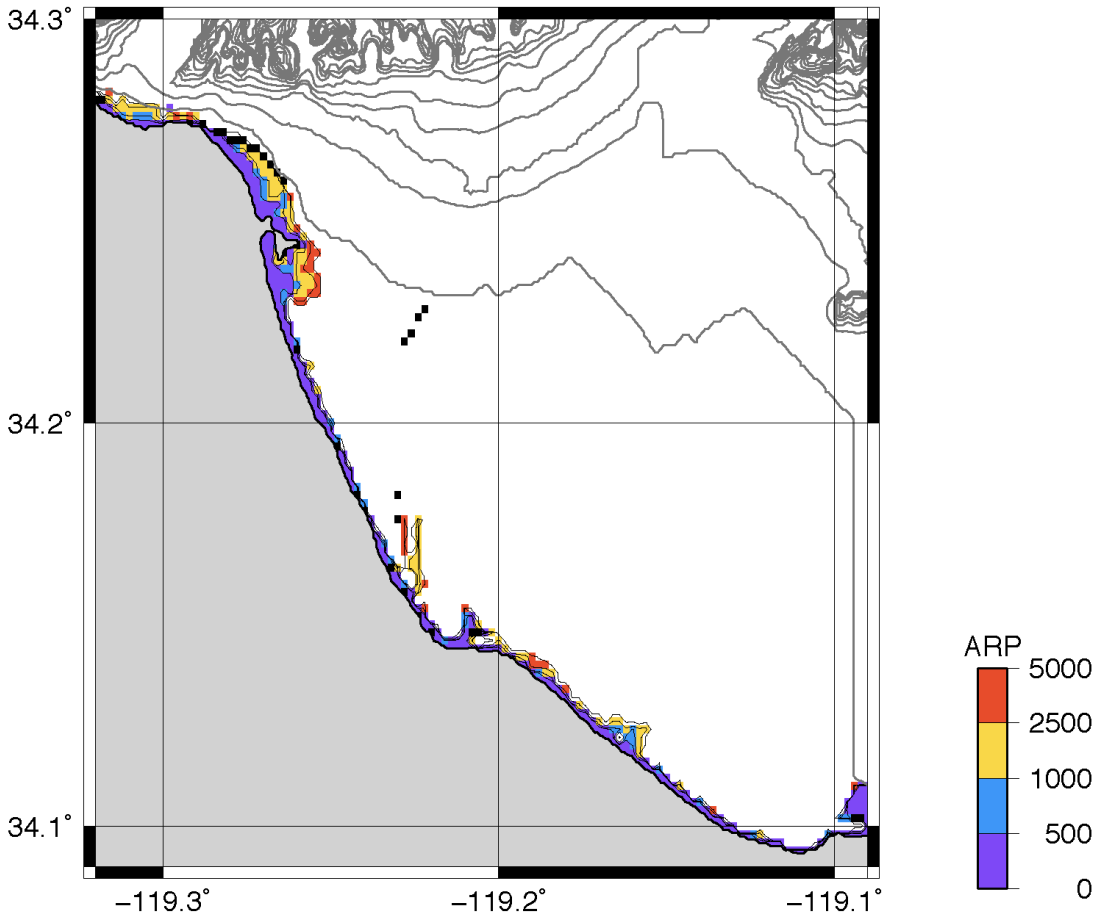

Figure 25 Probabilistic inundation map for the Ventura region.

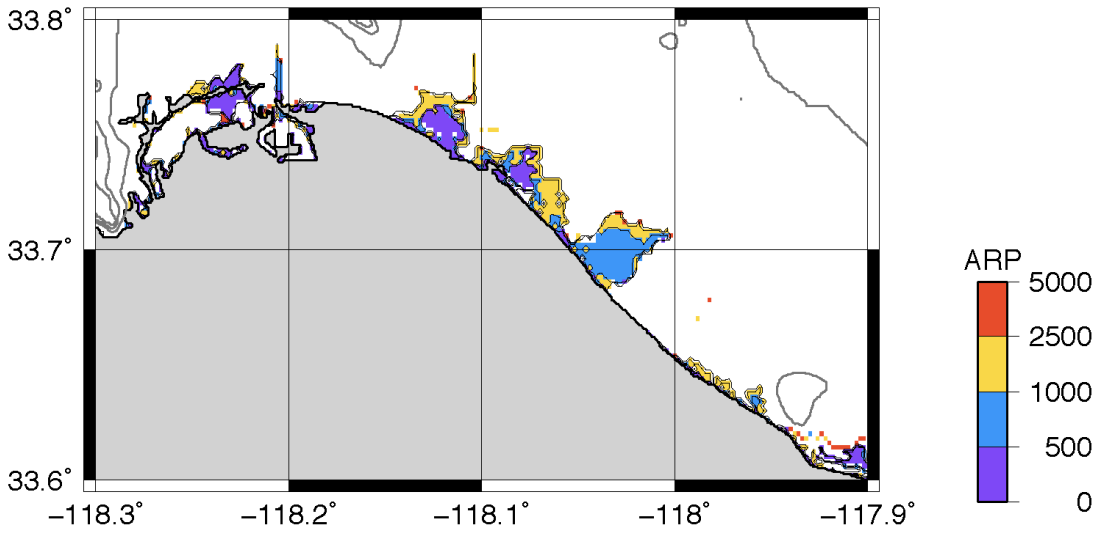

Figure 26 Probabilistic inundation map for Port of Los Angeles to Orange County.

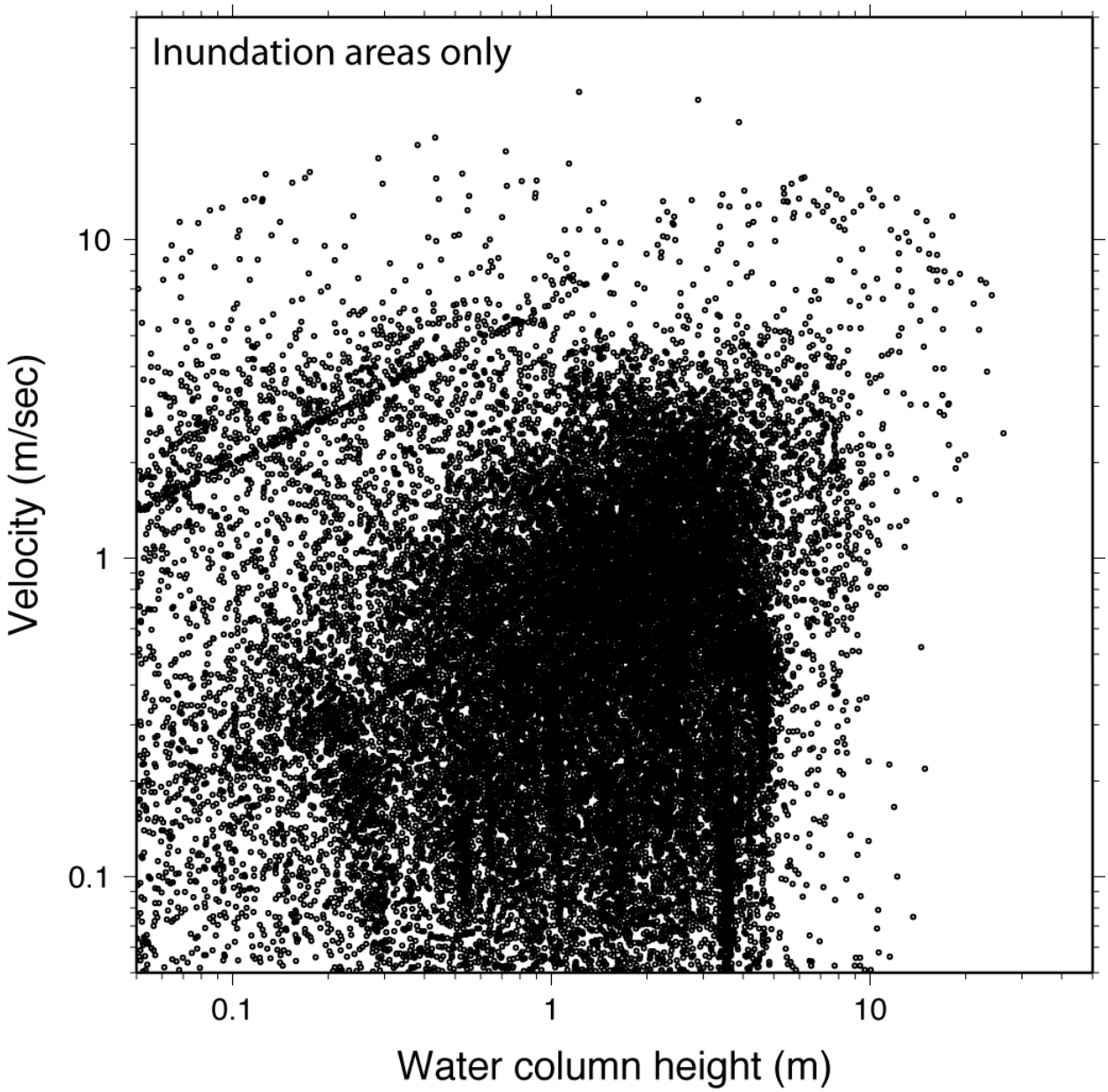

Figure 27 Relationship between flow velocity and water column height in inundated areas.

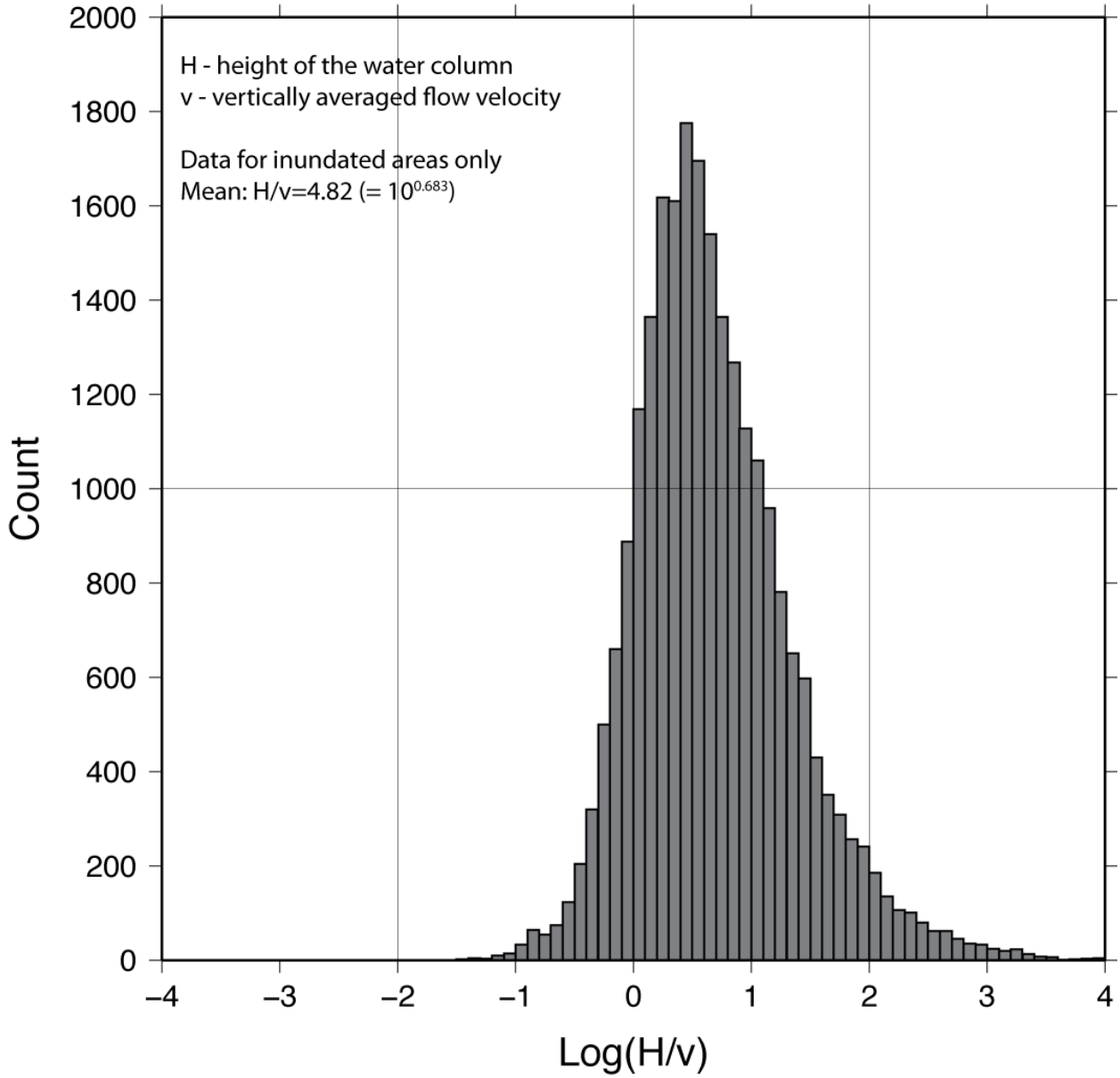

Figure 28 Distribution of the ratio between water column height and flow velocity.